Friction-induced planar vibration of a two-rigid-disc system with a finite contact area subjected to uncertain friction

Han Hu, Anas Batou, Huajiang Ouyang, Ningyu Liu

Friction-induced planar vibration of a two-rigid-disc system with a finite contact area subjected to uncertain friction

Han Hu[a], Anas Batou[a,b], Huajiang Ouyang[a,c], Ningyu Liu[d,*]

[a]*Department of Mechanical, Materials and Aerospace Engineering, School of Engineering, University of Liverpool, Liverpool L69 7ZF, United Kingdom*
[b]*MSME, Univ Gustave Eiffel, CNRS UMR 8208, Univ Paris Est Creteil, F-77474 Marne-la-Vallée, France*
[c]*Tribology Research Institute, Southwest Jiaotong University, Chengdu, 610031, China.*
[d]*School of Traffic and Transportation Engineering , Central South University, Changsha, 410075, China*

Abstract

Friction-induced vibration of mechanical systems has significant academic appeal and industrial implications. This paper presents a novel approach to studying the friction-induced planar vibrations of a two-rigid-disc system with a finite contact area. In this approach, a set of discrete two-dimensional LuGre models are introduced to calculate the dynamics of the system, eliminating the need for a stick-slip transition criterion required by static friction models. Complex eigenvalue analysis and transient dynamic analysis are performed to analyse the linear stability and bifurcation properties of the system. The spatial variation of the coefficient of friction is also considered, modelled for the first time as an interval field, and is found to greatly impact the system's stick-slip behaviour and cause oscillations around equilibrium points.

Keywords: Friction-induced vibration, Stability analysis, Nonlinear dynamics, LuGre model, Interval field

1. Introduction

Friction-induced vibration is a common phenomenon caused by relative motion between two surfaces in contact, resulting in self-excited vibration. The vibration can range from small, periodic oscillations to large, chaotic motions and can have adverse effects on a mechanical system, such as wear, noise, and energy loss. Over the years, researchers have identified four main mechanisms contributing to friction-induced vibration: (1) Negative friction slope [1, 2], where the coefficient of friction decreases with increasing relative velocity between surfaces, leading to self-excited friction and dynamic instability; (2) Mode coupling [3, 4], where the interaction of multiple vibration modes results in energy transfer between the modes and the emergence of new vibration frequencies; (3) The stick-slip motion [5, 6], where alternating states of stick and slip due to the non-smooth nature of dry friction causes system vibration; (4) The sprag-slip motion [7, 8]. The alternating engagement and release of the sprags can result in vigorous dynamic responses involving intermittent sticking and slipping phases.

*Corresponding author
Email address: liuningyu2015@hotmail.com (Ningyu Liu)

Nomenclature

Abbreviations

CEA Complex Eigenvalue Analysis

COF Coefficient of Friction

TDA Transient Dynamic Analysis

Symbols

γ_i Angle of ds_i with respect to the X_1 axis

$\mathbb{H}_{\mathrm{S}}^{\mathrm{I}}(\mathbf{X})$, $\mathbb{H}_{\mathrm{K}}(\mathbf{x})$ The static and kinetic coefficient of friction Interval fields

$\mathbf{F_f}$, $\mathbf{F}_{\mathbf{f}i}$ Global friction force and local friction forces

$\mathbf{P}i$, $\mathbf{Q}i$ Global coordinate of the centre of ds_i and its projection on the lower disc

$\mathbf{q}_{\mathrm{e}}$ The equilibrium point

$\mathbf{Z}$ Bristle deformation

μ_{S}, μ_{K} Static and kinetic coefficient of friction (COF)

Ω Driving angular velocity

ρ_i Distance from the centre of ds_i to O_1

σ_0, σ_1, σ_2 Stiffness coefficient, microscopic and macroscopic damping coefficients in the Lu-Gre model

Θ_e, Φ_{e} Circumferential displacement at the equilibrium point of the upper and lower discs

Θ, Φ Rotational displacement of the upper and lower discs

ξ_i^{I} Interval field coordinates

C_{p}, $C_{\mathrm{p}\Theta}$, C_{d}, $C_{\mathrm{d}\Phi}$ Damping terms for the translational and torsional motion of the upper and lower discs

ds_i Area of a small fraction of the cross-section of the connecting cylinder

F_{N} Constant normal load

H_{Sc}, H_{Sr} Interval centre and Interval radius of the static COF interval field

J_{p}, J_{d}, J_p, J_d Polar moment of inertia of the upper and lower discs

K_{p}, $K_{\mathrm{p}\Theta}$, K_{d}, $K_{\mathrm{d}\Phi}$ Stiffness of the translational and torsional springs connected to the upper and lower discs

M_{p}, M_{d} Mass of the upper and lower discs

R_1,R_2 Radius of the upper and lower discs

R_{c} Radius of the contact area

R_{d} Influence radius of the static COF interval field

T_Θ, T_Φ Torques generated by the friction forces of the upper and lower discs

V_{s} Stribeck velocity

$X_{1\mathrm{e}}$, $X_{2\mathrm{e}}$ Horizontal displacement at the equilibrium point of the upper and lower discs

$Y_{1\mathrm{e}}$, $Y_{2\mathrm{e}}$ Vertical displacement at the equilibrium point of the upper and lower discs

Investigating friction-induced vibration problems requires a suitable friction model to describe the underlying frictional behaviour. Over the years, various friction models have been developed, which can be categorised as either static or dynamic. Static models can be expressed as functions of friction force and relative velocity between contacting surfaces, such as the Coulomb's friction model and its modified versions [9, 10], velocity-based models [11] and the

Karnopp model [12]. These models are designed to describe the system behaviours in the steady state, at which the system has a large enough relative velocity. On the other side, dynamic friction models are capable of capturing dynamic effects in a wide range of relative velocity by the aid of inner state variables. The Dahl model [13] and the LuGre model [14] are typical dynamic friction models based on the conceptualisation of the deflection of flexible bristles, while the latter is an extension of the former incorporating the Stribeck effect [15]. The LuGre model has shown promising properties to replicate dynamics behaviours like pre-sliding, frictional lag and hysteresis effect and thus has widespread applications [16, 17]. Extensions to the LuGre model have also emerged such as the Elasto-plastic model [18] and the Leuven model [19]. Interested readers are referred to [20, 21] for an extensive overview of friction models. This work investigates friction-induced planar motions involving translational and rotational motions, and thus a friction model coping with 2D motion is in demand. Since a static model would require a complex 2D stick-slip transition criterion, which would degrade both efficiency and accuracy, the LuGre model is used instead for its simplicity and effectiveness in 2D motion. Applications of the LuGre model in 2D motion can be found in the literature, e.g. the distributed 2D LuGre tire friction model [22] and the lumped 2D LuGre model for point contact multi-body system [23].

Complex eigenvalue analysis (CEA) and transient dynamic analysis (TDA) are effective techniques for studying friction-induced vibration problems [24]. CEA, used in applications such as aeroelastic flutter [25] and brake squeal analysis [26], involves finding the equilibrium of the nonlinear system and linearising the system equations near this point to derive the stiffness and damping matrices. The eigenvalues of the linearised system are then calculated, and if any have a positive real part, the steady state is unstable and can result in self-excited vibrations. CEA is widely used in industry due to its computational efficiency and its ability to quickly identify unstable modes [27]. TDA, on the other hand, provides a detailed time response of the system's dynamic behaviour, including stick-slip effects and bifurcation [28, 24].

Friction-induced vibration problems have traditionally been studied using deterministic methods. However, recent advancements in the field include the study of uncertainty and variability in these systems. For instance, Butlin and Woodhouse [29] quantified the uncertainty and sensitivity of a friction-coupled system modelled with realistic complexity. Massa et al. [30] carried out a study using fuzzy approach for a friction-induced vibration problem to identify the unstable modes. Nechak and Sinou [31] constructed a hybrid meta-model taking into account random and interval uncertainties for the prediction of friction-induced instabilities. Nobari et al. [32] conducted CEA for a friction-induced vibration system in a statistical way to cope with variability and uncertainty of input variables for the stability analysis. Hu et al. [33, 34] proposed a random friction field modelling method in which the coefficient of friction is treated as a random field and the resulting frictional responses were analysed statistically. However, in practical engineering, the knowledge of the COF between certain materials is generally limited as only an interval of possible values, e.g. see [35, 36]. The limited information such as probability density function hinders the use of probabilistic approaches unless conducting a large number of measurements. A practical alternative is to model it as an interval field, where the required knowledge can be reduced to its upper and lower bounds and an influence radius indicating the spatial dependency of the variables. Interval field is analogous to random field, firstly proposed

by Moens et al. [37] and then developed into many variants, for instance, the K-L expansion based method [38] and the convex model based method [39]. Recently, a B-spline based interval field modelling method [40] is proposed by the authors, which has shown effectiveness and convenience to be constructed and is adopted to model the spatial variation of the coefficient of friction.

The present study investigates a two-rigid-disc system with a finite contact area and demonstrates the reliability of the friction model used in predicting its dynamical responses. A set of discrete 2D LuGre models, attached to each divided region of the discretised contact area, are used to calculate the frictional responses of the system. A combination of CEA and TDA is conducted to gain a comprehensive understanding of the system's stability and bifurcation properties. Finally, the variation of the coefficient of friction is studied by modelling it as an interval field to investigate its impact on the dynamical behaviour of the system. The rest of the paper is organised as follows. In Section 2, the friction-induced vibration of a two-rigid-disc system with finite contact area is discussed and the formulation of the discrete LuGre model is presented. Section 3 focuses on the stability and bifurcation analysis of the system through the use of Complex Eigenvalue Analysis (CEA) and Transient Dynamic Analysis (TDA). In Section 4, the non-deterministic friction model is introduced, including the examination of its effect on stick-slip behaviour and the deviation of the system's response from its deterministic counterpart.

2. Model description of a two-rigid-disc system

The present work investigates the friction-induced planar vibrations of a two-rigid-disc system. The model is an extension of the one used in [41] but with a finite contact area and subjected to non-deterministic friction, the latter of which will be discussed in Sec.4 in detail. The model is depicted in Fig.1, in which two circular discs interact through a cylindrical bar rigidly connecting to the edge of the upper disc and frictionally contacting with the lower disc. Both discs are elastically constrained by two springs in the direction of X_1 (or X_2) and Y_1 (or Y_2) and one torsional spring in the direction of Θ (or Φ). A constant vertical load F_N is applied normal to the upper disc. The vertical motions of both discs are constrained so that only planar vibrations will occur. The torsional spring of the lower disc is driven by an angular velocity Ω at one end and will cause the lower disc to spin around its centre O_2, which will eventually cause the vibration of the upper disc through the frictional contact. The initial coordinates of O_1 and O_2 are identical, and the initial X and Y axes attached to each disc are correspondingly parallel. The governing equations for the system can be stated as

$$\begin{cases} M_\mathrm{p}\,\ddot{X}_1 + C_\mathrm{p}\,\dot{X}_1 + K_\mathrm{p}\,X_1 = \mathbf{F_f}\cdot\mathbf{e}_\mathrm{x} \\ M_\mathrm{p}\,\ddot{Y}_1 + C_\mathrm{p}\,\dot{Y}_1 + K_\mathrm{p}\,Y_1 = \mathbf{F_f}\cdot\mathbf{e}_\mathrm{y} \\ J_\mathrm{p}\,\ddot{\Theta} + C_{\mathrm{p}\Theta}\,\dot{\Theta} + K_{\mathrm{p}\Theta}\,\Theta = T_\Theta \\ M_\mathrm{d}\,\ddot{X}_2 + C_\mathrm{d}\,\dot{X}_2 + K_\mathrm{d}\,X_2 = -\mathbf{F_f}\cdot\mathbf{e}_\mathrm{x} \\ M_\mathrm{d}\,\ddot{Y}_2 + C_\mathrm{d}\,\dot{Y}_2 + K_\mathrm{d}\,Y_2 = -\mathbf{F_f}\cdot\mathbf{e}_\mathrm{y} \\ J_\mathrm{d}\,\ddot{\Phi} + C_{\mathrm{d}\Phi}\,\dot{\Phi} + K_{\mathrm{d}\Phi}\,\Phi = T_\Phi \end{cases}, \tag{1}$$

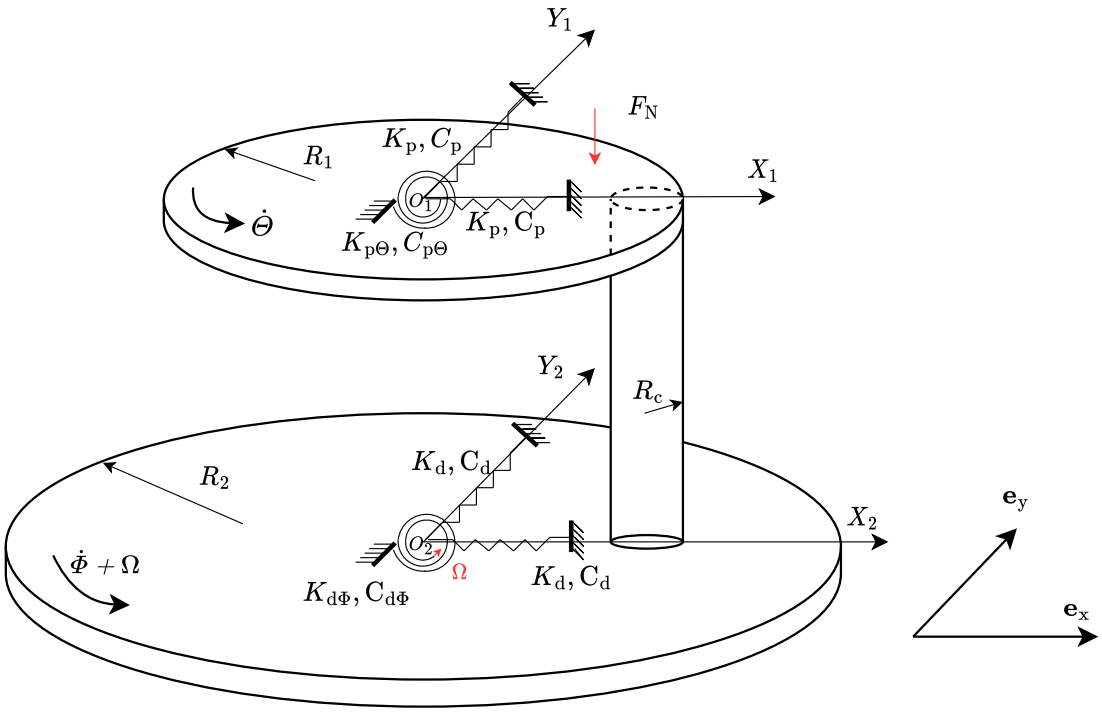

Fig. 1. The two-rigid-disc system setting.

where $M_{\mathrm{p}}, J_{\mathrm{p}}$ denote the mass and polar moment of inertia of the upper disc, $K_{\mathrm{p}}, K_{\mathrm{p}\Theta}$ denote the stiffness of the translational and torsional springs connected to the upper disc and $C_{\mathrm{p}}, C_{\mathrm{p}\Theta}$ are the damping terms. Correspondingly, $M_{\mathrm{d}}, J_{\mathrm{d}}, K_{\mathrm{d}}, K_{\mathrm{d}\Phi}, C_{\mathrm{d}}, C_{\mathrm{d}\Phi}$ are the parameters for the lower disc, as indicated in Figure 1. The global coordinate system uses $\mathbf{e}_{\mathrm{x}}$ and $\mathbf{e}_{\mathrm{y}}$ as its two orthogonal basis vectors. Friction forces are indicated by $\mathbf{F_f}$ and the torques generated by these forces T_Θ, T_Φ, of which the calculation entails discretising the contact interface, e.g. the bottom cross-section of the connecting cylinder, as shown in Figure 2. The contact surface has been discretised. In the local coordinate of the upper disc, a small fraction of the cross-section of an area ds_i ($\sum_i ds_i = \pi R_{\mathrm{c}}^2$, R_{c} is the radius of the contact cross-section) has a distance ρ_i from its centre to O_1 and an angle γ_i with respect to the X_1 axis. In this work, a mesh size of 0.20 is adopted considering the computational efficiency and convergence analysis. A convergence analysis with respect to the mesh size can be found in Appendix A. The global coordinate of the centre of this small fraction $\mathbf{P}_i = (P_{i\mathrm{X}}, P_{i\mathrm{Y}})$ and its absolute velocity $\dot{\mathbf{P}}_i = (\dot{P}_{i\mathrm{X}}, \dot{P}_{i\mathrm{Y}})$ can be represented as

$$\begin{cases} P_{i\mathrm{X}} = X_1 + \rho_i \cos(\gamma_i + \Theta) \\ P_{i\mathrm{Y}} = Y_1 + \rho_i \sin(\gamma_i + \Theta) \\ \dot{P}_{i\mathrm{X}} = \dot{X}_1 - \rho_i \sin(\gamma_i + \Theta)\, \dot{\Theta} \\ \dot{P}_{i\mathrm{Y}} = \dot{Y}_1 + \rho_i \cos(\gamma_i + \Theta)\, \dot{\Theta}. \end{cases} \tag{2}$$

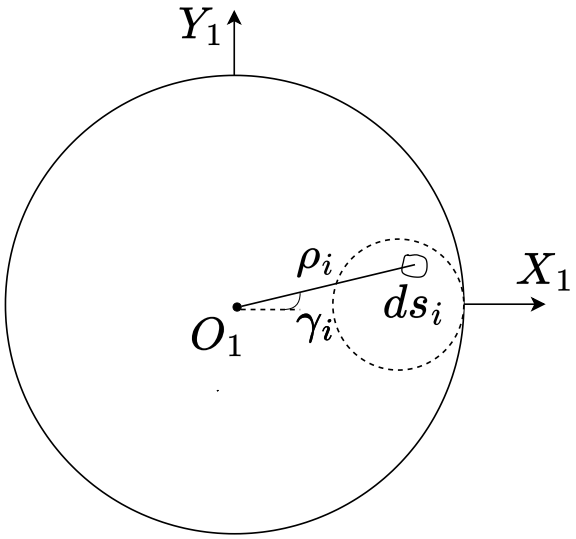

Fig. 2. A small fraction of the cross-section of the cylindrical bar.

Such a small area is in contact with the lower disc, of which the velocity of the centre of the contact area $\mathbf{Q}_i = (Q_{i\mathrm{X}}, Q_{i\mathrm{Y}})$ can be represented as

$$\begin{cases} \dot{Q}_{i\mathrm{X}} = \dot{X}_2 - (P_{i\mathrm{Y}} - Y_2)\,\dot{\Phi} \\ \dot{Q}_{i\mathrm{Y}} = \dot{Y}_2 + (P_{i\mathrm{X}} - X_2)\,\dot{\Phi}. \end{cases} \tag{3}$$

The relative velocity between points $\mathbf{P}_i$ and $\mathbf{Q}_i$ is then determined as $\mathbf{V}_{\mathrm{r}i} = (\dot{P}_{i\mathrm{X}} - \dot{Q}_{i\mathrm{X}}, \dot{P}_{i\mathrm{Y}} - \dot{Q}_{i\mathrm{Y}})$. The friction force $\mathbf{F}_{\mathbf{f}i} = (F_{fi\mathrm{X}}, F_{fi\mathrm{Y}})$ is computed using a set of discrete 2D LuGre models. The LuGre model is a dynamical friction model, illustrated in Fig.3, which is known for its effectiveness in describing dynamical friction behaviours and convenience in implementation. The LuGre model considers the microscopic interactions between contacting asperities as a set of elastic bristles with damping. The friction force is then represented by the average deflection of those bristles. In the amended form of the LuGre model [42], auxiliary state variables $\mathbf{Z}_i = (Z_{iX}, Z_{iY})$ are introduced to determine the dynamical evolution of the friction force, represented as

$$\begin{cases} \dot{\mathbf{Z}}_i = \mathbf{V}_{\mathrm{r}i} - \mathbf{Z}_i \,\frac{\sigma_0 |\mathbf{V}_{\mathrm{r}i}|}{G(\mathbf{Q}_i, \Phi, \mathbf{V}_{\mathrm{r}i})} \\ G(\mathbf{V}_{\mathrm{r}i}) = \mu_{\mathrm{K}} + (\mu_{\mathrm{S}} - \mu_{\mathrm{K}})\, \mathrm{e}^{-|\mathbf{V}_{\mathrm{r}i}/V_{\mathrm{s}}|^2} \\ \mathbf{F}_{\mathbf{f}i} = -(\sigma_0\, \mathbf{Z}_i + \sigma_1\, \dot{\mathbf{Z}} + \sigma_2\, \mathbf{V}_{\mathrm{r}i})\, F_{\mathrm{N}}, \end{cases} \tag{4}$$

where σ_0 is a constant parameter denoting the stiffness coefficient of the bristle, σ_1, σ_2 represent the microscopic and macroscopic damping coefficients, respectively. μ_{S} and μ_{K} denote the static and kinetic COF, and V_{s} is the Stribeck velocity.

An advantage of the LuGre model is that an explicit stick-slip transition criterion is no longer required as it is incorporated implicitly into the model by the state variables. Such a criterion is essential in static models and it often requires a careful treatment to ensure accuracy [34]. The friction-related terms in (1) can thus be derived as the

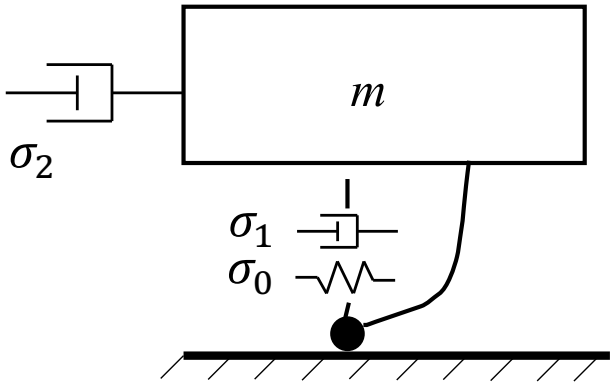

Fig. 3. The LuGre model.

composition of local friction forces as

$$\begin{cases} \mathbf{F}_i = \Sigma_i \, \mathbf{F}_{\mathbf{f}i} \\ T_\Theta = \Sigma_i \left[F_{fi\mathrm{Y}} \, \rho_i \, \cos(\gamma_i + \Theta) - F_{fi\mathrm{X}} \, \rho_i \, \sin(\gamma_i + \Theta) \right] \\ T_\Phi = \Sigma_i \left[-F_{fi\mathrm{Y}} \, (P_{i\mathrm{X}} - X_2) + F_{fi\mathrm{X}} \, (P_{i\mathrm{Y}} - Y_2) \right]. \end{cases} \tag{5}$$

To obtain the system dynamics, equations (4) and (5) are substituted into the governing equations (1). It should be noted that the friction forces and torques make the problem highly nonlinear. Moreover, incorporating the discrete LuGre model results in a stiff system, as the frequency in the stick state is much higher than in the slip state [43]. Therefore, choosing an appropriate solver that can handle both challenges is crucial, as an insufficient solver could lead to many iterations in one time step or cause convergence issues. In this work, the MATLAB multistep stiff solver *ode15s* is adopted, which is based on the numerical differentiation formulas of orders 1 to 5 [44] and has shown to provide satisfactory results in practice.

3. Deterministic stability analysis and bifurcation analysis of the system

3.1. Complex eigenvalue analysis

In this section, the stability analysis of the two-rigid-disc system is carried out. In the first step, the equilibrium point of the system is sought by eliminating all differential terms in (1) and (4). The following nonlinear algebraic equations are thus established as

$$\mathbf{K}\mathbf{q}_\mathrm{e} = \mathbf{b}, \tag{6}$$

where $\mathbf{K} = \mathrm{diag}\{K_\mathrm{p}, K_\mathrm{p}, K_{\mathrm{p}\Theta}, K_\mathrm{d}, K_\mathrm{d}, K_{\mathrm{d}\Phi}\}$ is the stiffness matrix, $\mathbf{q}_\mathrm{e} = \{X_{1\mathrm{e}}, Y_{1\mathrm{e}}, \Theta_e, X_{2\mathrm{e}}, Y_{2\mathrm{e}}, \Phi_\mathrm{e}\}^\mathrm{T}$ is the equilibrium point and $\mathbf{b} = [b_1, b_2, b_3, b_4, b_5, b_6]^\mathrm{T}$, the components $b_i \, (i = 1, 2, ..., 6)$ are expressed in Appendix B. The right-hand side vector $\mathbf{b}$ is a function of $\mathbf{q}_\mathrm{e}$. As a consequence, Eq.(6) is highly nonlinear and requires a nonlinear solver. After obtaining the equilibrium point of the system, the Complex Eigenvalue Analysis (CEA) is performed to study the stability of the system around that equilibrium point. The system equations (1) should be linearised in the following

form as

$$\mathbf{M}_{\mathrm{l}}\,\ddot{\mathbf{q}} + \mathbf{C}_{\mathrm{l}}\,\dot{\mathbf{q}} + \mathbf{K}_{\mathrm{l}}\,\mathbf{q} = 0, \tag{7}$$

where $\mathbf{M}_{\mathrm{l}} = \mathrm{diag}\{M_{\mathrm{p}}, M_{\mathrm{p}}, J_p, M_{\mathrm{d}}, M_{\mathrm{d}}, J_d\}$, $\mathbf{C}_{\mathrm{l}} = \mathrm{diag}\{C_{\mathrm{p}}, C_{\mathrm{p}}, C_{\mathrm{p}\Theta}, C_{\mathrm{d}}, C_{\mathrm{d}}, C_{\mathrm{d}\Phi}\} - \partial\mathbf{b}/\partial\mathbf{q}\,|_{\mathbf{q}=\mathbf{q}_{\mathrm{e}}}$ and $\mathbf{K}_{\mathrm{l}} = \mathbf{K} - \partial\mathbf{b}/\partial\mathbf{q}\,|_{\mathbf{q}=\mathbf{q}_{\mathrm{e}}}$. The components in $\mathbf{C}_{\mathrm{l}}$ and $\mathbf{K}_{\mathrm{l}}$ are provided in Appendix C. In the theory of CEA, the eigenvalues of the linearised system (7) indicate the stability of the equilibrium point: all negative real parts of eigenvalues indicate stability while the presence of at least one eigenvalue possessing positive real part indicates instability.

In the numerical simulations of the current and the following sections, the same parameters reported in Table 1 are used unless otherwise stated.

Table 1: Parameters used for simulation

M_{p} [kg]	J_{p} [kg · m^2]	M_{d} [kg]	J_{d} [kg · m^2]	K_{p} [N · m^{-1}]	$K_{\mathrm{p}\Theta}$ [N · rad^{-1}]	K_{d} [N · m^{-1}]	$K_{\mathrm{d}\Phi}$ [N · rad^{-1}]
1	0.5	4	8	10	10	100	100
C_{p} [Ns · m^{-1}]	$C_{\mathrm{p}\Theta}$ [Ns · rad^{-1}]	C_{d} [Ns · m^{-1}]	$C_{\mathrm{d}\Phi}$ [Ns · rad^{-1}]	V_{s} [m · s^{-1}]	σ_0 [m^{-1}]	σ_1 [s · m^{-1}]	σ_2 [s · m^{-1}]
0.1	0.1	0.1	0.1	0.001	10^5	$\sqrt{10^5}$	0.01
μ_{S}	μ_{K}	R_1 [m]	R_2 [m]				
0.4	0.32	1.0	2.0				

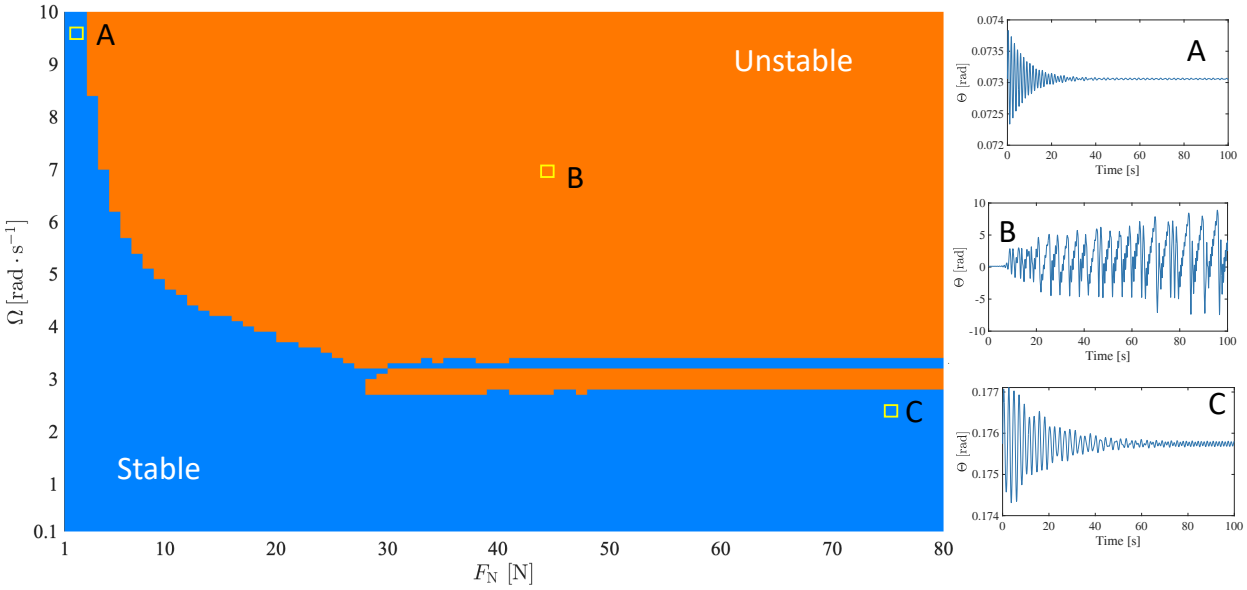

Fig. 4. Stability analysis of the equilibrium points for $R_{\mathrm{c}} = 0.10$ [m]. Left: stability map. Right: circumferential responses of the upper disc for three cases.

The stability of the equilibrium points with $R_{\mathrm{c}} = 0.10$ [m] with the variation of normal load F_{N} (equispaced by 1) and driving angular velocity Ω (equispaced by 0.1) is obtained and shown in Fig.4. It can be observed that although

irregular patterns occur in the diagram, the areas of stable and unstable parameters can be approximately split by a boundary curve from up left to the bottom right. To further examine the validity of the result, three pairs of (F_N, Ω) parameters (marked A, B and C in Fig.4) are used to compute the dynamical response of the circumferential vibration of the upper disc starting from the vicinity of the equilibrium point under those parameters. Pair A (F_N = 2 [N], Ω = 9.7 [rad/s]) is a stable case and the dynamical response converges to the equilibrium point Θ_e = 0.0731 [rad]. Pair C (F_N = 76 [N], Ω = 2.3 [rad/s]) is another stable case in which the dynamical response oscillates around its equilibrium point Θ_e = 0.1216 [rad] with a reducing magnitude. In comparison, the parameter pair B (F_N = 45 [N], Ω = 7 [rad/s]) is obtained as an unstable case, and the dynamical response indeed shows an increasing osicillation amplitude with the simulation time, which means the response rapidly deviates from the equilibrium point Θ = 0.120 [rad] as time increases and thus is certainly not stable. The responses of the three cases mentioned above illustrate the result of the CEA.

A second investigation is carried out to determine how the contact area's size will affect the system's stability. Varying R_c and keeping other parameters unchanged, the stability maps of the system can be obtained and are shown in Fig.5. In Fig.5(a) the point contact case is presented for comparison, in which the system becomes unstable after increasing the normal load to a certain level around 25 [N]. It can be observed that with the increase of the contact

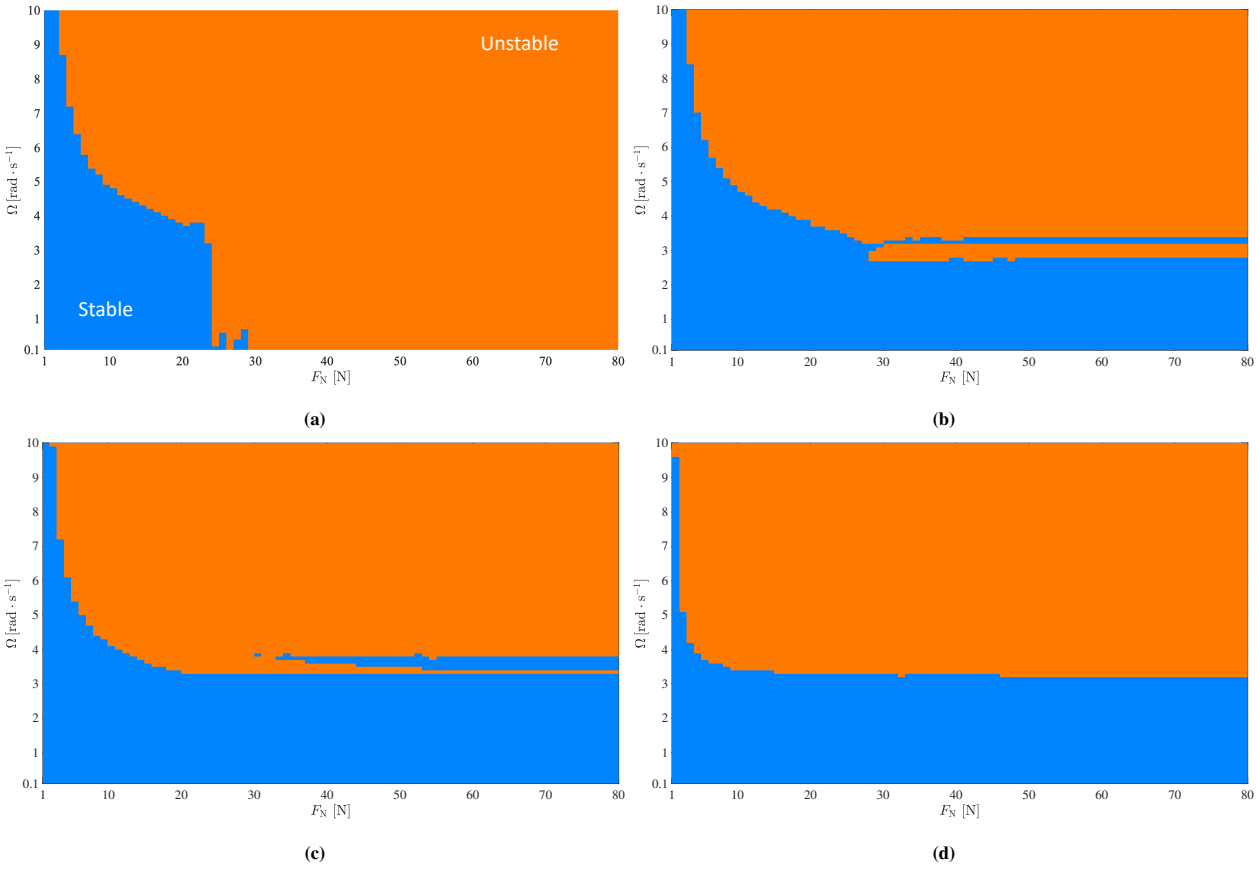

Fig. 5. Stability maps with (a) point contact; (b) R_c = 0.10 [m]; (c) R_c = 0.30 [m]; (d) R_c = 0.50 [m].

area, parameters that lead to a stable equilibrium point concentrate in the lower part of the diagram, where the critical

driving angular velocity sits between 3-4 [rad $\cdot$ s^{-1}]. The critical value of Ω is seen to lift up slightly with an expanding contact area. For a low normal load, the stable areas greatly decrease when R_c increases, meaning a large contact area between the two discs will prevent a stable equilibrium point at a low normal load and a high driving angular velocity.

It is commonly believed that systems with higher damping tend to be more stabilising [45]. Hence, the effect of the separate viscous damping (indicated by '$C_\square$') on the stability of the system is then studied. In Table 1, all viscous damping terms have the same value of 0.1. Their values will be changed simultaneously to another value indicating a different damping level, indicated by C. As shown in Fig.6, the stability of the system with $R_c = 0.10$ [m] with four damping levels corresponding to values taken from $\{0.0, 0.1, 0.2, 0.5\}$, are investigated through CEA. It should

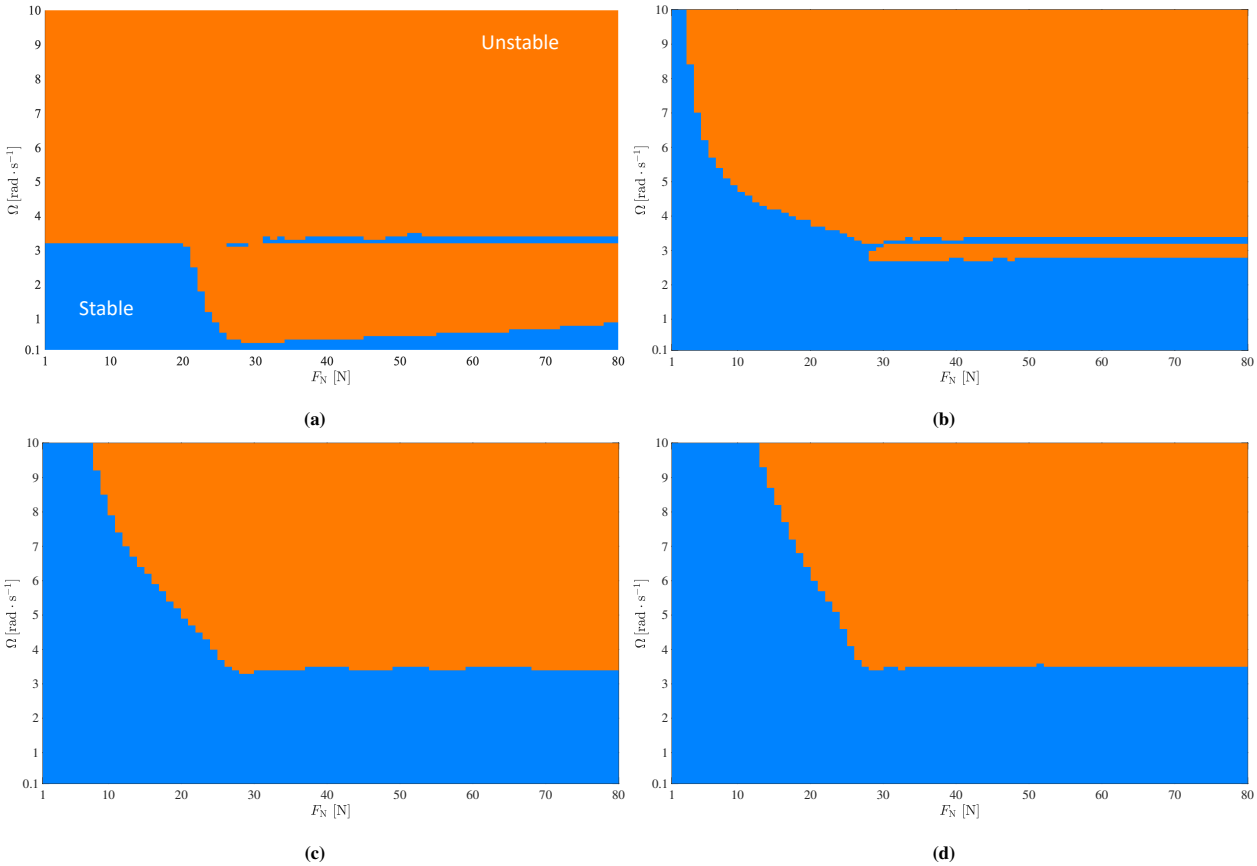

Fig. 6. Stability maps with $R_c = 0.10$ [m] and damping level (a) $C = 0$; (b) $C = 0.10$; (c) $C = 0.30$; (d) $C = 0.50$.

be noted that varying the viscous damping level will not change the equilibrium point. In the case where there is no viscoelastic damping, the stable area is mainly limited in the left bottom corner of the diagram and is significantly smaller than in other cases. In comparison, strengthening the damping level simultaneously can effectively enlarge the stable area, especially in regions with low normal loads and high rotational speed.

3.2. Bifurcation analysis

After drawing a general picture of the system's stability in the previous section, the transient dynamics of the system under specific control parameters are investigated. The system's bifurcation behaviour is of particular interest

as the Hopf bifurcation point indicates the transformation of the motion status. In what follows, the normal load and the driving angular velocity are chosen as the control parameters. Different scenarios are investigated by varying the contact area or the damping level of the system. All simulations in this section start at the all-zeros initial condition, and the extreme (maximum and minimum) values of circumferential displacement of the upper disc are recorded when the system enters the steady state.

The bifurcation diagram for varying F_{N} is shown in Fig.7. For the point contact case, it can be seen that the Hopf bifurcation point locates at around $F_{\mathrm{N}} = 20$ [N], beyond which the system stops converging to the equilibrium point and a stable limit cycle shows up. The radius of the limit cycle expands as the normal load increases until F_{N} is larger than 70 [N], after which the limit cycle maintains the same level. It can also be noticed that the Hopf bifurcation points shift to the left when the contact area increases, which means that the system can have a limit cycle at a low normal load when enlarging the contact area. In the meantime, the radius of the limit cycle behaves oppositely with the radius of the contact area. Figure 8 illustrates the system bifurcation diagram where the driving angular velocity is set as the

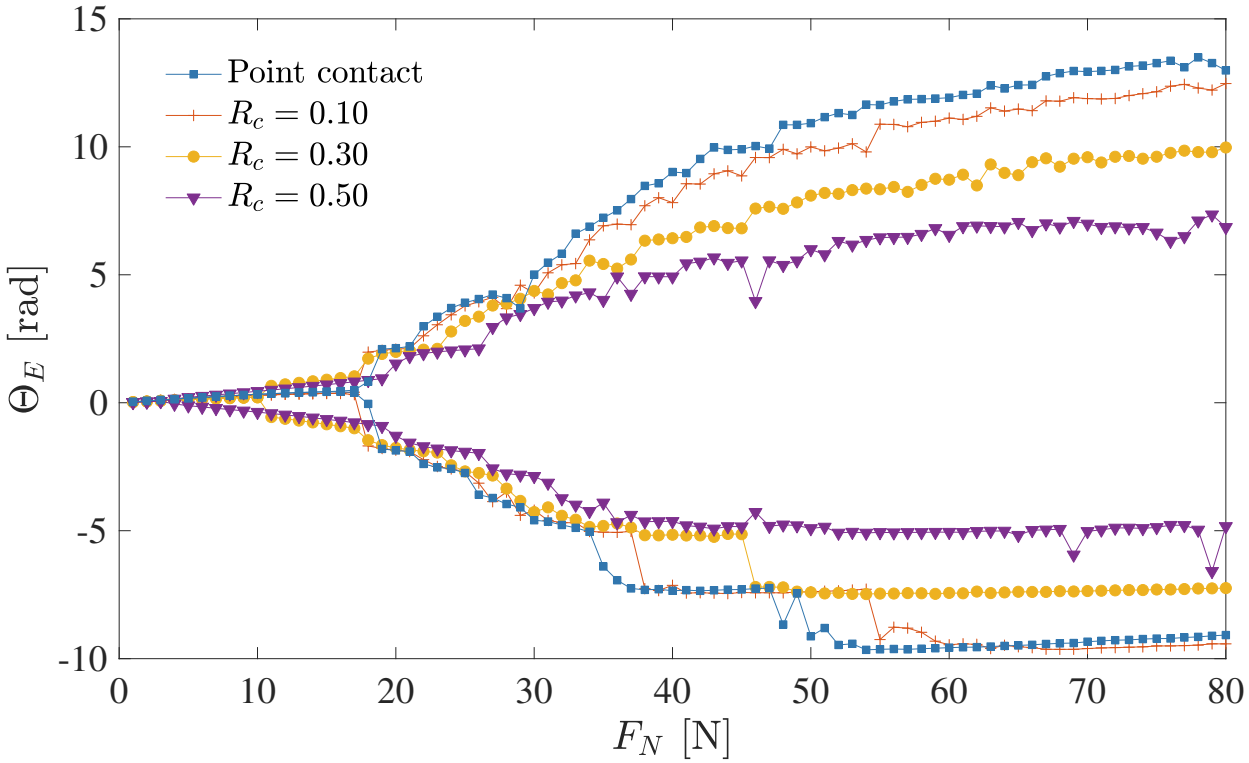

Fig. 7. Bifurcation diagram for $\Omega = 4$ [rad $\cdot$ s^{-1}] and $C = 0.1$.

control parameter while the normal load and damping level are constants as $F_N = 50$ [N] and $C = 0.1$. For the three scenarios studied with different finite contact areas, the resulting Hopf bifurcation points locate closely to each other between $\Omega \in [3, 4]$ [rad $\cdot$ s^{-1}]. When Ω continues to increase over the Hopf bifurcation points, a stable equilibrium point disappears and a stable limit cycle shows up. The radius of the limit cycle again increases with the decrease of the contact area at a given driving angular velocity. In contrast, for the point contact case, no stable equilibrium point exists under this condition, so its extreme values split from the beginning of the variation of the control parameter.

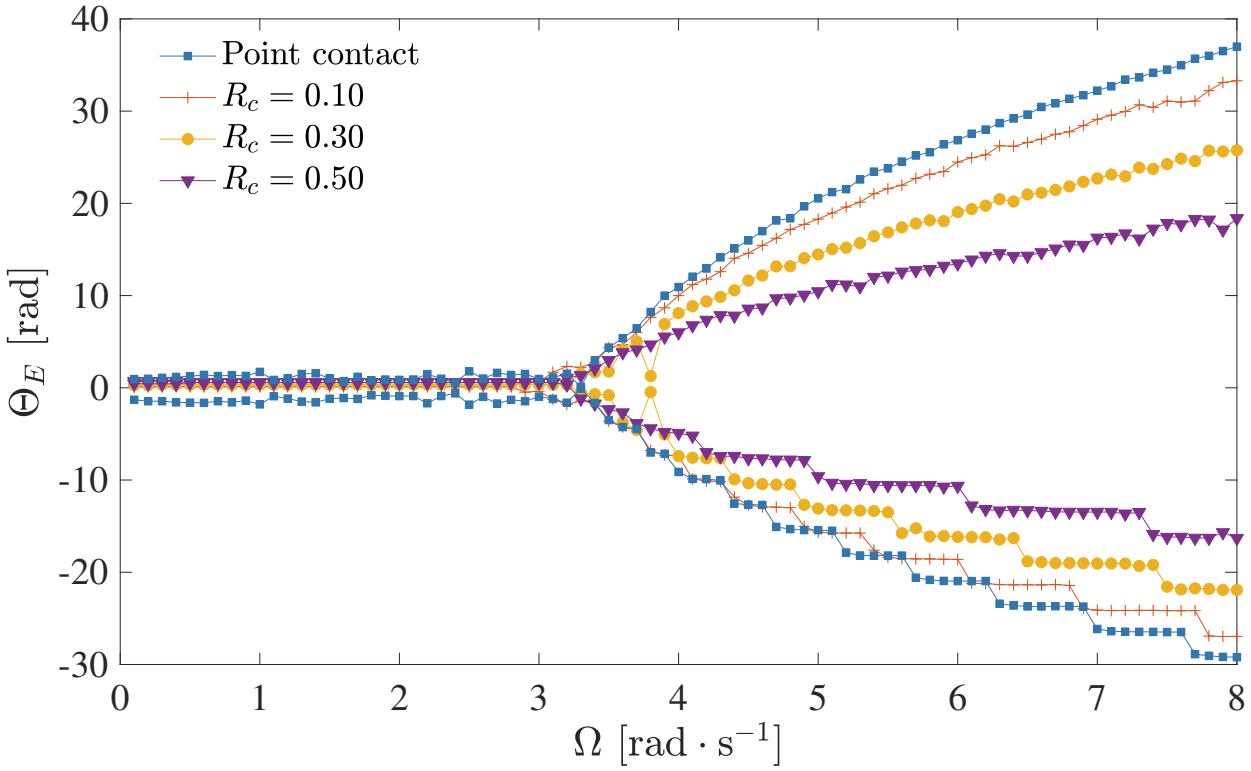

Fig. 8. Bifurcation diagram for F_N = 50 [N] and C = 0.1.

In the last case, the impact of the damping level on the system's bifurcation behaviours is studied, as shown in Fig.9, where the normal load is the control parameter and Ω and R_c are set as constants. It can be clearly observed that the Hopf bifurcation points shift to the right when increasing the damping level, enlarging the region where a stable equilibrium point exists. In the meantime, the radius of the limit cycle shrinks under a large damping level, indicating a weakening oscillation at the steady state. Note that the locations of the Hopf bifurcation points are consistent with the stable-unstable boundary on the corresponding stability maps shown in the previous section, thus demonstrating the reliability of the dynamical responses.

4. Non-deterministic analysis with a coefficient of friction interval field

In the aforementioned study, the friction force and torque were assumed to be deterministic due to the treatment of the coefficient of friction as a constant. However, previous experimental measurements of coefficient of friction have shown that it can not be considered as a fixed value and is inherently uncertain [46, 47]. In practical engineering applications, the exact value of the coefficient of friction at a contact interface is often uncertain and can only be estimated within upper and lower bounds [35, 36]. When addressing surface contact problems, the coefficient of friction at different local contact points may vary, while close contact points may have similar values. In such situations, it is appropriate to model the coefficient of friction of the entire contact interface as an interval field.

In this section, the non-deterministic nature of the coefficient of friction at the contact interface is taken into

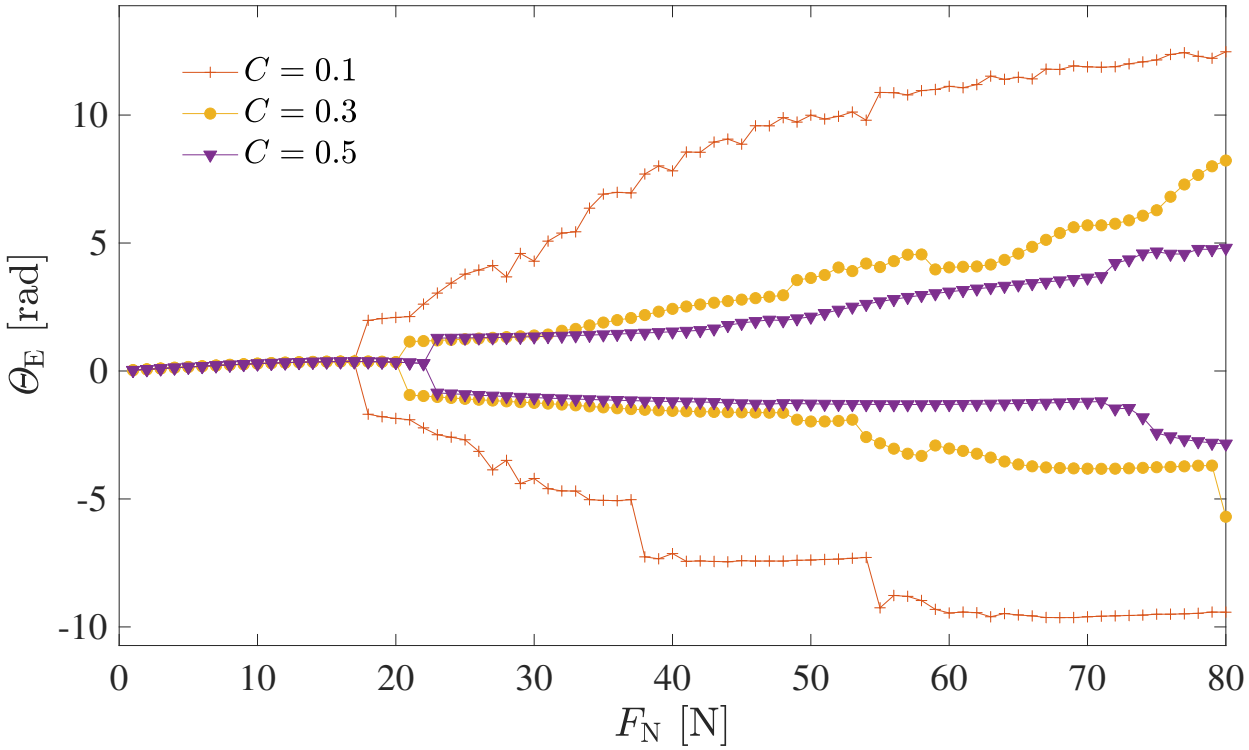

Fig. 9. Bifurcation diagram for $\Omega = 4$ [rad $\cdot$ s^{-1}] and $R_c = 0.10$ [m].

consideration, and it is modelled as an interval field. The interval field, defined by crisp bounds and a dependency length, is used to investigate its impact on the system performance. The coefficient of friction is no longer uniform across the contact interface, but instead varies depending on local contact properties such as roughness. For the sake of simplicity, the bottom surface of the connecting cylinder is assumed to be smooth while the top surface of the lower disc is rough. Thus, the coefficient of friction interval field can be constructed based on the properties of the lower disc alone. While both surfaces could be considered as rough, doing so would increase the required algorithmic complexity without significantly changing the results. Additionally, an ideal assumption of isotropic coefficient of friction is adopted, meaning that the local coefficients of friction in the x- and y-directions are considered the same.

This interval field can be represented as $\{\mathbb{H}_S^I(\mathbf{X}), \mathbf{X}$ in the domain of lower disc$\}$ and is constructed using the recently proposed B-spline interval field decomposition method [40], which has an explicit formulation to account for the spatially-dependent uncertainty as

$$\mathbb{H}_S^I(\mathbf{X}) = H_{Sc} + H_{Sr} \sum_{i=1}^{N} B_i(\mathbf{X})\, \xi_i^I, \tag{8}$$

where H_{Sc} and H_{Sr} represent, respectively, the interval centre and interval radius of the static COF interval field so that the static COF only varies within $[H_{Sc} - H_{Sr}, H_{Sc} + H_{Sr}]$. The set $\{B_i(\mathbf{X}), i = 1, ..., N\}$ contains two-dimensional quadratic B-spline functions built on the spatial domain of the lower disc incorporating the influence radius R_d, which is used to decide the spatial dependency of the field variables, and $\{\xi_i\}$ denote *Interval Field Coordinates* (IFCs) taking values in the interval [-1, 1]. An elaboration of the interval field modelling method can be found in [40]. The local

kinetic COF is treated as a scaled static COF interval field as $\mathbb{H}_{\mathrm{K}}(\mathbf{x}) = \tau\,\mathbb{H}_{\mathrm{S}}(\mathbf{x})$, where $\tau = 0.8$ is a constant scaling factor [34]. Figure 10 exhibits two realisations of the static COF interval field within the interval $[0.3, 0.5]$ in the spatial domain of the lower disc (of a radius $R_2 = 2$ [m]) with an influence radius $R_{\mathrm{d}} = 0.1$ [m]. Incorporating the concept of the COF interval field, the derivation of the friction force using the LuGre model is modified as

$$\begin{cases} \dot{\mathbf{Z}}_i = \mathbf{V}_{\mathrm{r}i} - \mathbf{Z}_i \frac{\sigma_0 |\mathbf{V}_{\mathrm{r}i}|}{G(\mathbf{Q}_i, \Phi, \mathbf{V}_{\mathrm{r}i})} \\ G(\mathbf{Q}_i, \Phi, \mathbf{V}_{\mathrm{r}i}) = \mathbb{H}_{\mathrm{K}}(\mathbf{Q}_i, \Phi) + (\mathbb{H}_{\mathrm{S}}(\mathbf{Q}_i, \Phi) - \mathbb{H}_{\mathrm{K}}(\mathbf{Q}_i, \Phi))\, \mathrm{e}^{-|\mathbf{V}_{\mathrm{r}i}/V_{\mathrm{s}}|^2} \\ \mathbf{F}_{\mathbf{f}i} = -(\sigma_0\, \mathbf{Z}_i + \sigma_1\, \dot{\mathbf{Z}} + \sigma_2\, \mathbf{V}_{\mathrm{r}i})\, F_{\mathrm{N}}, \end{cases} \tag{9}$$

in which case function $G(\mathbf{Q}_i, \Phi, \mathbf{V}_{\mathrm{r}i})$ now becomes not only relative velocity dependent but also position dependent.

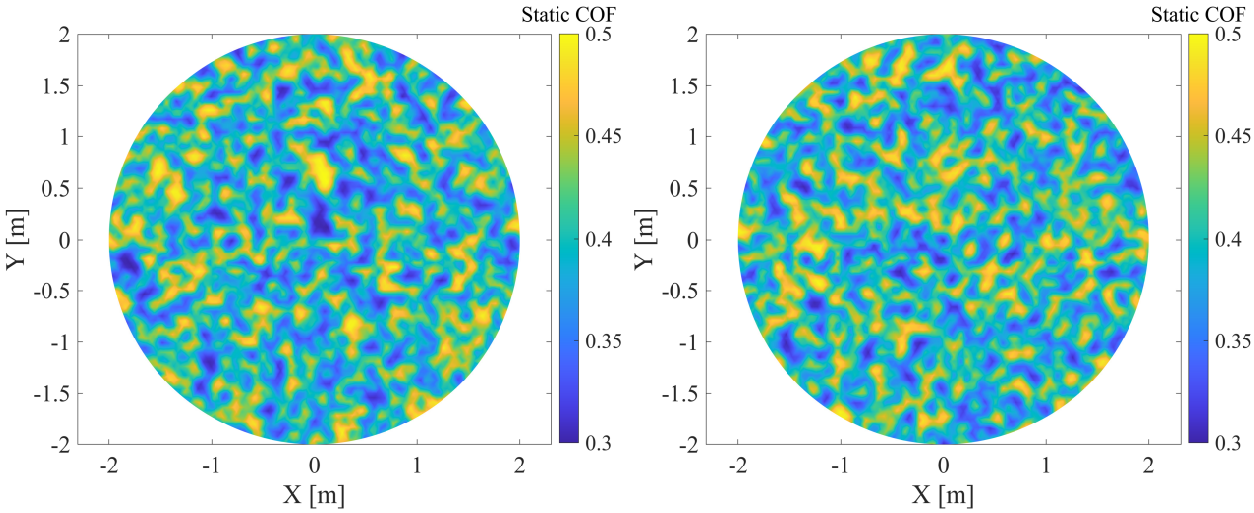

Fig. 10. Two realisations of the static COF interval field.

4.1. Stick-slip effect

Stick-slip effect depicts the self-sustained vibration occurring between two contacting bodies when their relative velocity is sufficiently low. In this section, the dynamical behaviours of the system are investigated under low driving angular velocity, e.g. $\Omega \in [0.001, 0.1]$ [rad $\cdot$ s^{-1}] for both the deterministic system and the non-deterministic system. For example, Figure 11(a) displays the time response of relative circumferential velocity between the upper and lower discs at $F_{\mathrm{N}} = 10$ [N] and $\Omega = 0.01$ [rad $\cdot$ s^{-1}] of the deterministic system, in which intermittent (almost) zero velocity can be observed indicating that contact between the two discs being at the state of stick. During the state of stick, no relative motion occurs between the two discs on the macroscopic scale, while microscopic relative motion is allowed since the relative velocity is not exactly zero at the state of stick due to the nature of the LuGre model. The phase portrait, shown in Fig.11(b), exhibits quasi-periodic behaviours of the upper disc when it enters the steady state. In contrast, when the driving angular velocity is increased to 0.10 [rad $\cdot$ s^{-1}], the stick-slip effects of the system disappear, as can be seen in Fig.12. Its phase portrait finally converges to a point under such a condition.

Based on the findings of the study, a grid analysis was conducted to determine the appearance of the stick-slip effect under specified control parameters. The normal load was sampled from each integer between 1 and 50 [N], and

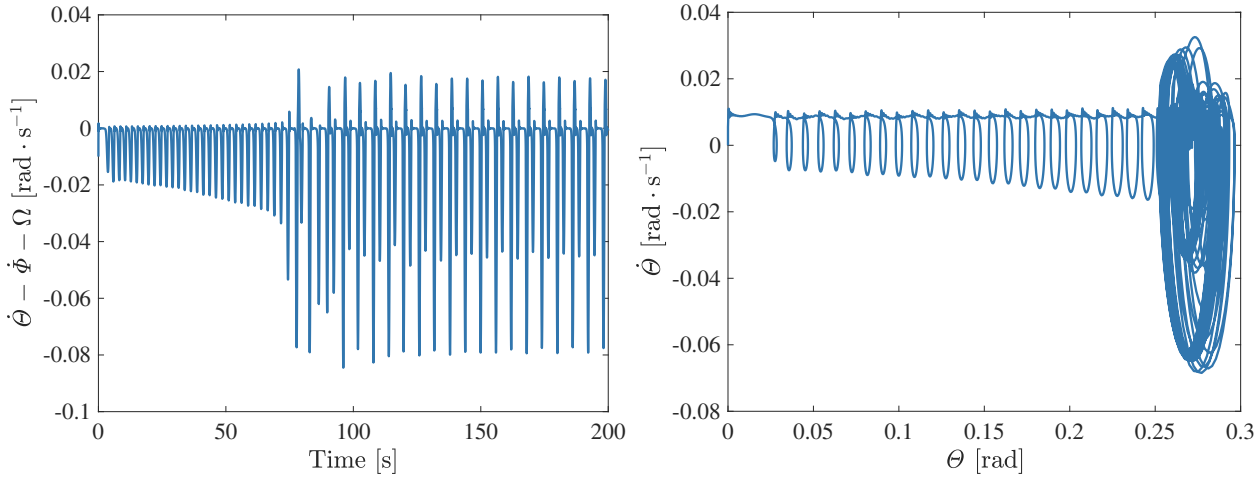

(a) **(b)**

Fig. 11. Dynamical results for the deterministic system at $F_N = 10$ [N], $\Omega = 0.01$ [rad · s^{-1}], $R_c = 0.10$ [m] (a) time response of relative circumferential velocity; (b) phase portrait of the upper disc.

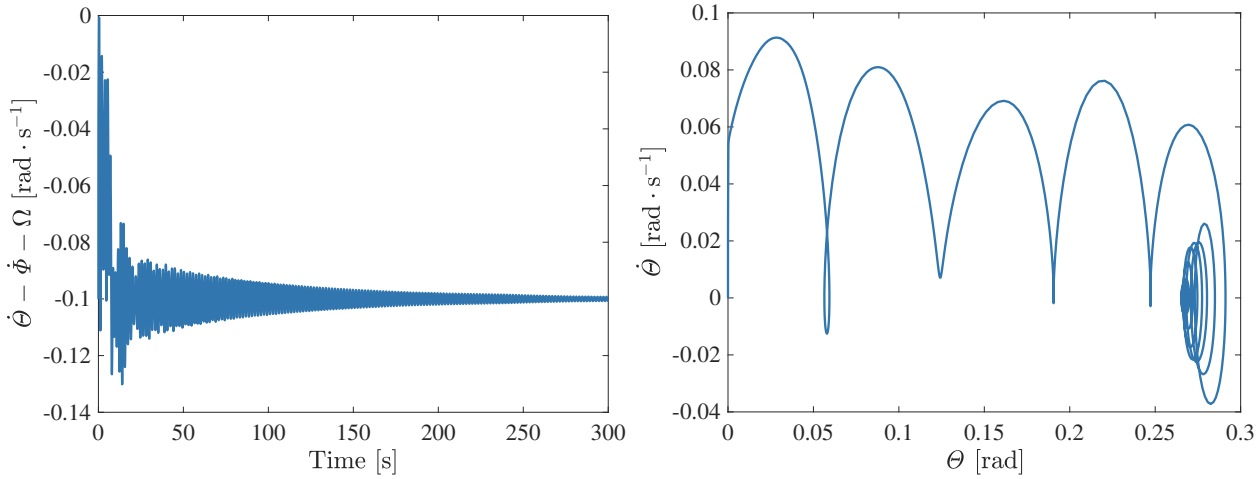

(a) **(b)**

Fig. 12. Dynamical results for the deterministic system at $F_N = 10$ [N], $\Omega = 0.10$ [rad · s^{-1}], $R_c = 0.10$ [m] (a) time response of relative circumferential velocity; (b) phase portrait of the upper disc.

the driving angular velocity was sampled from 0.001 to 0.1 rad/s, spaced equally by 0.001 [rad $\cdot$ s^{-1}]. The results are shown in Fig.13. It is observed that an increase in normal load leads to an increase in the maximum driving angular velocity that allows for the stick-slip effect to occur. The boundary between the "no stick-slip" region and the "stick-slip" region appears as a strip rather than a distinct line. The strip is wider at high normal loads compared with low normal loads. The control parameters within the strip lead to partial stick-slip behaviour: stick-slip behaviour appears initially, but cannot be sustained and eventually decreases to reach the equilibrium point as time evolves. A sample case is provided in Fig.14(a), where the relative circumferential velocity oscillates but reaches zero values around the first 60 [s], after which it never returns to zero and gradually stops oscillating.

In comparison, as shown in Fig.13(b), the maximum driving angular velocities that allow for the stick-slip effect to occur in the non-deterministic system are generally higher than in the deterministic system. The variation of the coefficient of friction increases the oscillation of the results and prevents the system from reaching the equilibrium point to some extent. Consequently, the same control parameters that can not sustain the stick-slip effect in the deterministic system may lead to a sustainable stick-slip effect in the non-deterministic system, as illustrated in Fig.14(b). Such a finding is consistent with the results in the literature [48]. It should be noted that the stick-slip stability map of the non-deterministic system is obtained using a single realisation of the COF interval field. Different realisations may result in subtle changes to the map, but the conclusion remains unchanged.

4.2. Interval analysis

In the stick-slip analysis, it has been found that the spatial variation of the COF leads to the oscillation of the dynamic responses, which may prevent the response of the system from converging to the equilibrium point (calculated from the deterministic model) even though the equilibrium point is stable. As shown in Fig.15, in a steady state the responses of the deterministic model in both small and large contact areas converge to the corresponding equilibrium points, while those of the interval field model have strong oscillations and are not decaying over time. In addition, it can be found that the responses of the interval model with a large contact area show lower oscillating amplitude than those with a small contact area.

Interval analysis has been carried out to quantify the deviation bounds of the interval model's time-domain responses to their deterministic counterparts using the normal load as the control parameter. Two cases with large (R_c = 0.50 [m]) and small (R_c = 0.10 [m]) contact areas are studied. The driving angular velocity is fixed at Ω = 1 [rad $\cdot$ s^{-1}] during the analysis so that from Fig.5(b) one can see under most variations of the normal load, the systems have stable equilibrium points. The extreme values of circumferential displacement of the upper disc are recorded when the system enters into the steady state. For the interval field model, 1000 Monte-Carlo simulations are performed, with each lasting 300 [s] of simulation time. The results are presented in Fig.16. A few findings should be pointed out from these results. Firstly, the equilibrium points of the deterministic model with a small contact area have a local maximum approximately at F_N = 20 [N], while those of the deterministic model with a large contact area increase monotonically with normal loads. Secondly, in most cases, the extreme values Θ_E of the deterministic results are single-valued (the maximum value equalling the minimum value), which means the time responses converge to the equilibrium points. The extreme values Θ_E of the deterministic results of the model with a small contact area separate

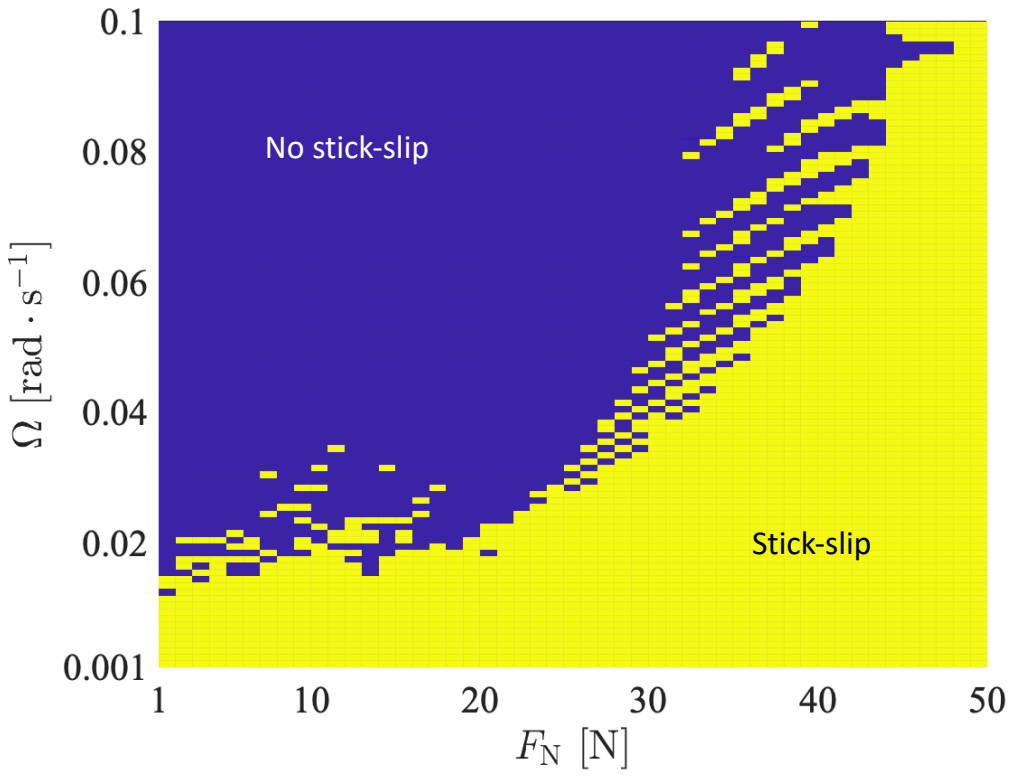

(a)

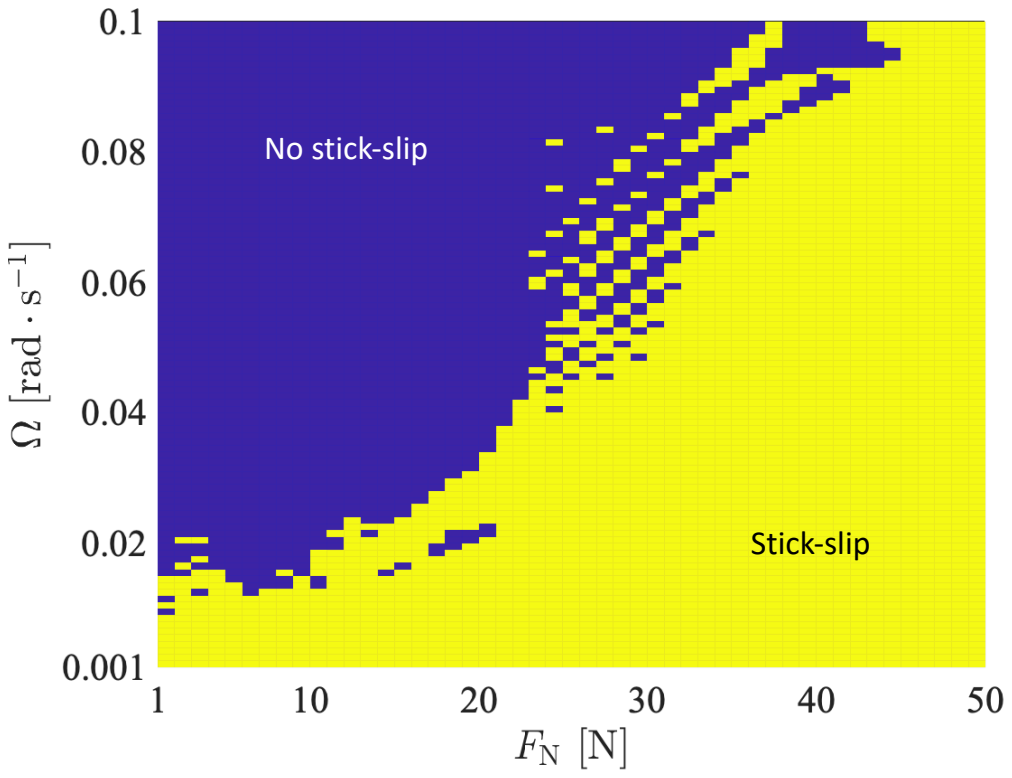

(b)

Fig. 13. Stick-slip stability maps for R_c = 0.10 [m]. (a) Deterministic system; (b) non-deterministic system.

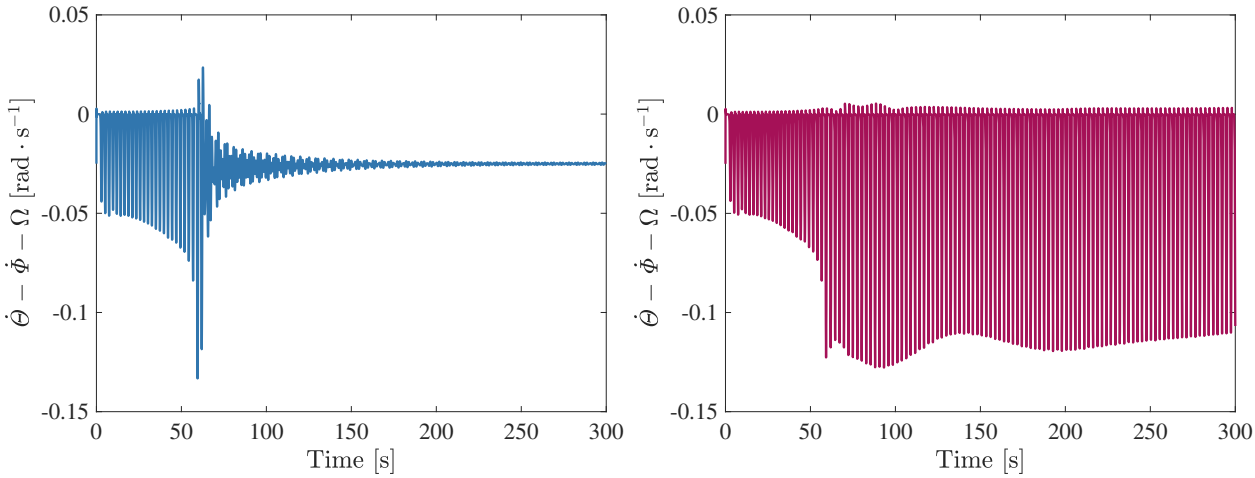

Fig. 14. Time response of relative circumferential velocity at $F_N = 20$ [N], $\Omega = 0.025$ [rad · s^{-1}], $R_c = 0.10$ [m] for (a) deterministic system; (b) non-deterministic system.

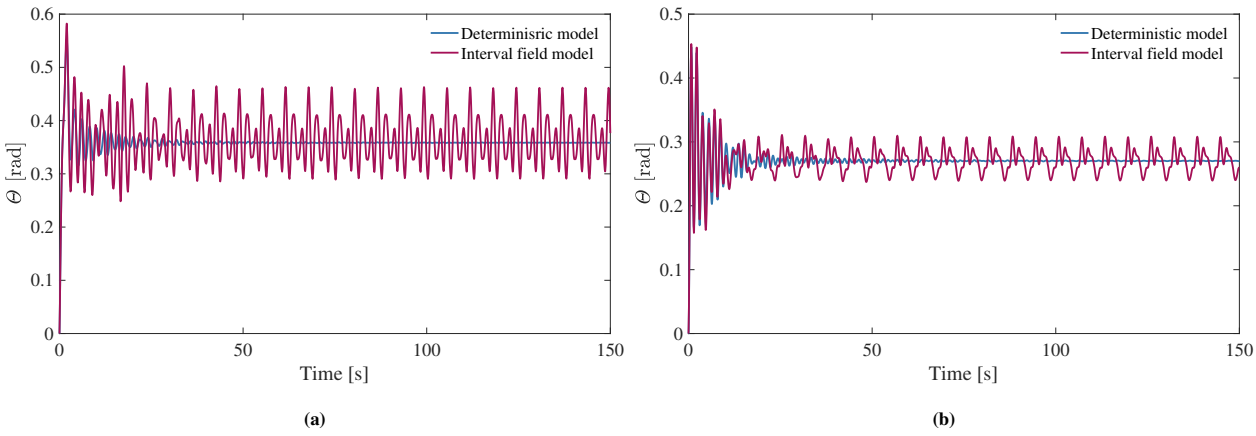

Fig. 15. Transient dynamic responses of Θ at $F_N = 20$ [N], $\Omega = 1$ [rad · s^{-1}] for (a) $R_c = 0.10$ [m] and (b) $R_c = 0.50$ [m].

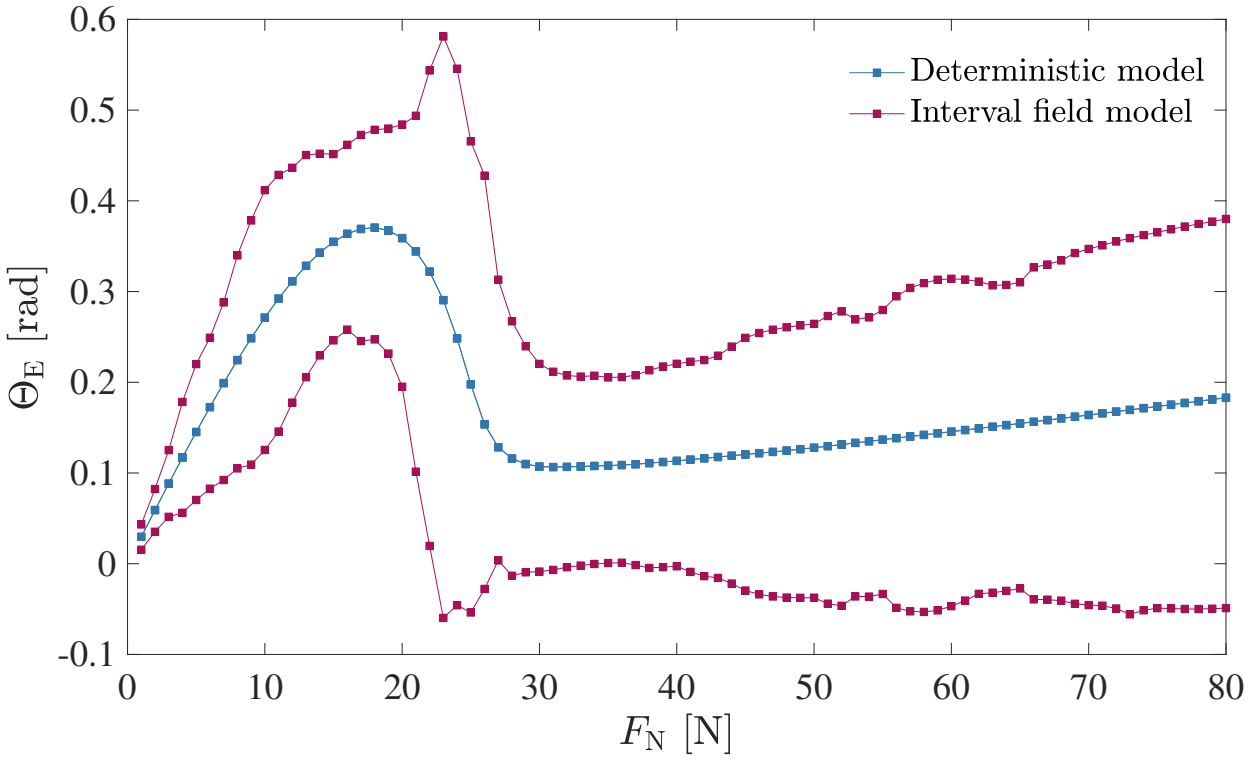

(a)

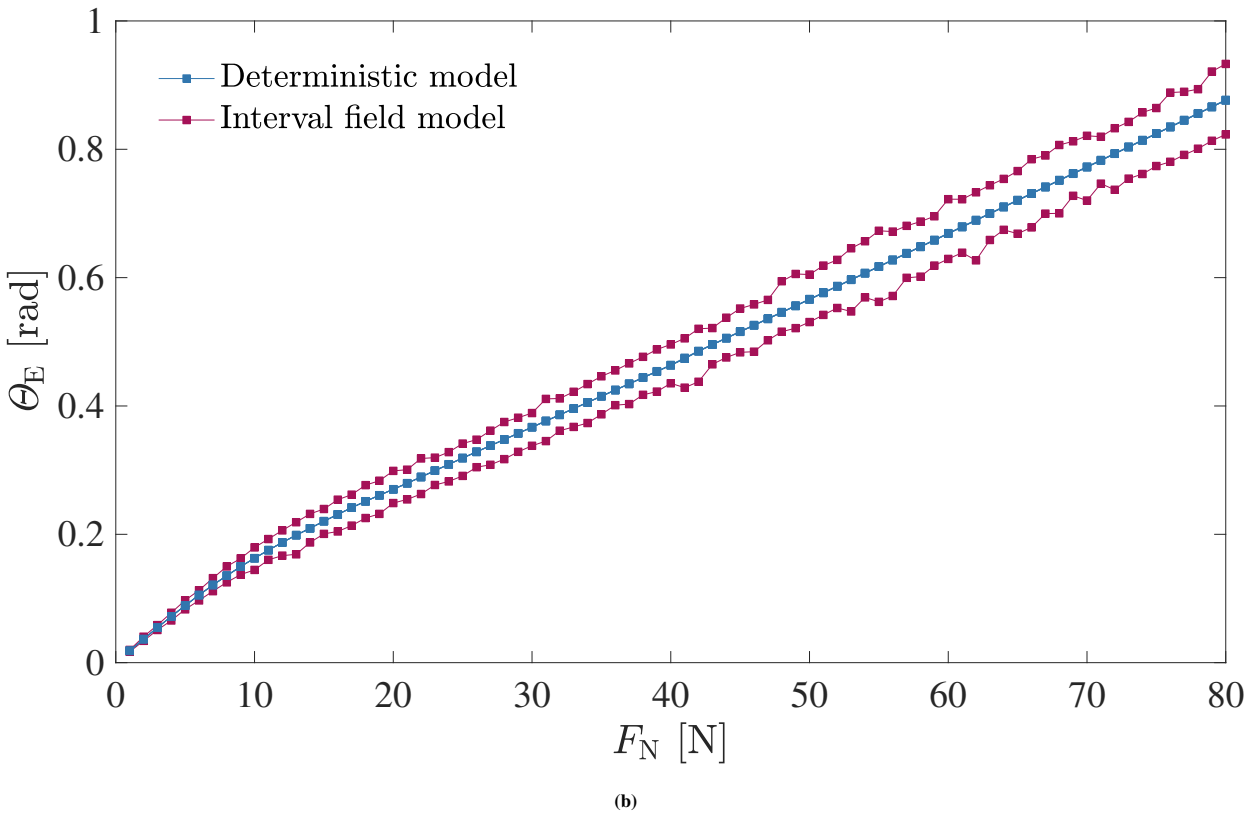

(b)

Fig. 16. Interval analysis of deviation from deterministic results at $\Omega = 1$ [rad $\cdot$ s^{-1}] for (a) $R_c = 0.10$ [m] and (b) $R_c = 0.50$ [m].

at around $F_N = 60$ [N], showing unstable equilibrium points in the nearby region, which is consistent with the stability analysis results shown in Fig.5(b). Thirdly, the results of the interval field model enclose the corresponding deterministic results and the deviations are relatively smaller under a small normal load compared with deviations under a large one. Finally, the deviations between the results of the interval field model and the deterministic model with a large contact area are significantly smaller compared with those of both models with a small contact area, which means that enlarging the contact area may eliminate or at least weaken the impact of variation of the coefficient of friction.

5. Conclusions

This paper studies the friction-induced vibration problems of a two-rigid-disc system with a finite contact area. A set of discrete LuGre models are used to facilitate the calculation of system dynamics, thus avoiding defining an explicit stick-slip transition criterion like required by static friction models. The system is analysed using complex eigenvalue analysis and transient dynamic analysis to study the stability and bifurcation behaviour. The results show that changes in contact area and damping level can significantly impact the stability and bifurcation diagrams, with the Hopf bifurcation point shifting in response. The second part of the paper considers uncertainties in friction by modelling the coefficient of friction as an interval field. The results show that considering these uncertainties can result in increased stick-slip effects and a wider range of control parameters that can lead to these behaviours. Additionally, increasing the contact area is found to weaken the effect of variations in the coefficient of friction. Future work should aim for an extended experimental validation.

Acknowledgment

Hu gratefully acknowledges the financial support from the University of Liverpool and China Scholarship Council Awards (CSC NO.201906230311). Dr Ningyu Liu participated in the initial stage of this research while he was studying for PhD at Liverpool and guided the research after his departure.

Authors' contributions

Conceptualization: Ningyu Liu, Han Hu; **Methodology**: Han Hu, Ningyu Liu; **Formal analysis and investigation**: Han Hu, Ningyu Liu; **Writing - original draft preparation**: Han Hu; **Writing - review and editing**: Ningyu Liu, Anas Batou, Huajiang Ouyang; **Funding acquisition**: Huajiang Ouyang; **Supervision**: Anas Batou, Huajiang Ouyang.

Funding

Ouyang has received research support from the National Natural Science Foundation of China (12272324).

Data availability

The datasets generated during and/or analysed during the current study are available from the corresponding author on reasonable request.

Code availability

The computer code used in generating the numerical results in this paper can be disclosed upon reasonable request and agreement of a proper acknowledgment of the code.

Competing Interests

The authors have no relevant financial or non-financial interests to disclose.

Appendix A Convergence analysis

The finite contact area is discretised by the triangular element of a mesh size h. Friction forces are imposed on the mass centre of each discretised area and their magnitudes are decided by the area. In the following content, a convergence analysis with respect to the mesh size is studied. The dynamics of the system is calculated under the default setting (parameters shown in Table 1) with the radius of the contact area $R_c = 0.10$ [m], normal load $F_N = 20$ [N] and driving angular velocity $\Omega = 1.0$ [rad/s]. The dynamics calculated using a very fine mesh ($h/R_c = 0.001$) is taken as a reference result. The relative error of the circumferential displacement of the upper plate is calculated using the following formulation

$$\mathrm{Err} = \frac{\int |\Theta - \Theta_{\mathrm{ref}}|^2 \, \mathrm{d}t}{\int |\Theta_{\mathrm{ref}}|^2 \, \mathrm{d}t} \tag{A.1}$$

It is clear from the result, shown in Fig.A.1, that the relative error converges as the mesh size decreases. Specifically, when the mesh size ratio h/R_c is below 0.30, the dynamics of the system becomes comparable with that of the reference case. On the basis of the convergence analysis, a mesh size ratio $h/R_c = 0.20$ is set for all simulations of this paper.

Appendix B Force components at equilibrium point

$$b_1 = \sum_i F_{fi\mathrm{Xe}}, \tag{B.1}$$

$$b_2 = \sum_i F_{fi\mathrm{Ye}}, \tag{B.2}$$

$$b_3 = \sum_i [F_{fi\mathrm{Ye}} \rho_i \cos(\gamma_i + \Theta_{\mathrm{e}}) - F_{fi\mathrm{Xe}} \rho_i \sin(\gamma_i + \Theta_{\mathrm{e}})], \tag{B.3}$$

$$b_4 = -\sum_i F_{fi\mathrm{Xe}}, \tag{B.4}$$

$$b_5 = -\sum_i F_{fi\mathrm{Ye}}, \tag{B.5}$$

$$b_6 = \sum_i [-F_{fi\mathrm{Ye}} X_{\mathrm{e}i} + F_{fi\mathrm{Xe}} Y_{\mathrm{e}i}]\}^{\mathrm{T}}, \tag{B.6}$$

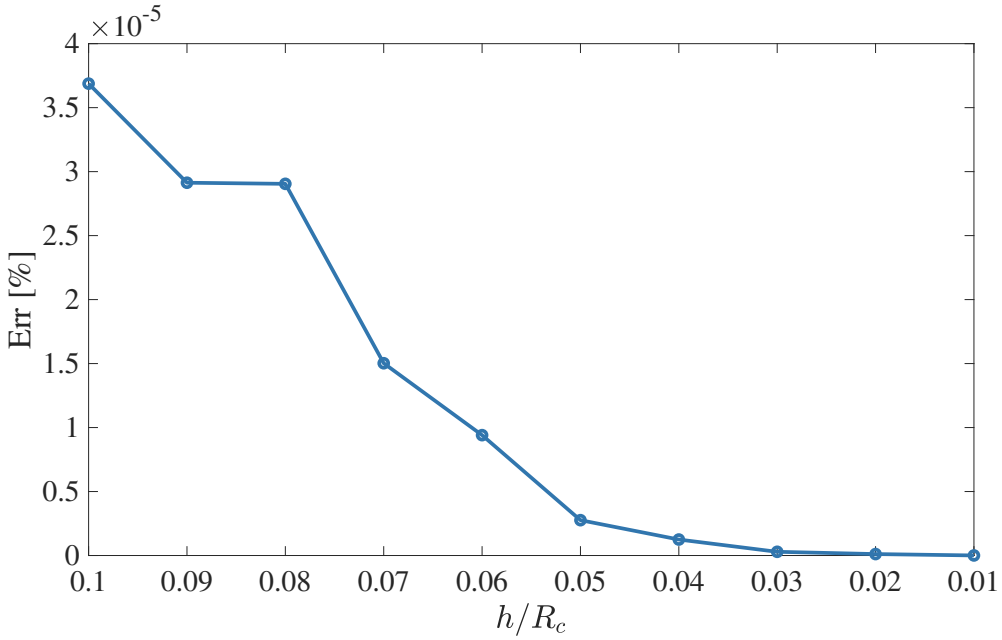

Fig. A.1. Convergence analysis w.r.t mesh size. $R_c = 0.10$ [m], $F_N = 20$ [N], $\Omega = 1.0$ [rad/s] and simulation time $t = 30$ [s].

where

$$F_{fi\mathrm{Xe}} = -N_i\,(\frac{V_{ri\mathrm{X}}G_\mathrm{e}}{V_{ri\mathrm{e}}} + \sigma_2 V_{ri\mathrm{X}}), \tag{B.7}$$

$$F_{fi\mathrm{Ye}} = -N_i\,(\frac{V_{ri\mathrm{Y}}G_\mathrm{e}}{V_{ri\mathrm{e}}} + \sigma_2 V_{ri\mathrm{Y}}), \tag{B.8}$$

$$N_i = \frac{F_\mathrm{N}}{\pi R_\mathrm{c}^2}\mathrm{d}s_i, \tag{B.9}$$

$$X_{ei} = X_{1\mathrm{e}} - X_{2\mathrm{e}} + \rho_i\cos(\gamma_i + \Theta_\mathrm{e}), \tag{B.10}$$

$$Y_{ei} = Y_{1\mathrm{e}} - Y_{2\mathrm{e}} + \rho_o\sin(\gamma_i + \Theta_\mathrm{e}), \tag{B.11}$$

$$V_{ri\mathrm{X}} = \Omega\,Y_{ei}, \tag{B.12}$$

$$V_{ri\mathrm{Y}} = -\Omega\,X_{ei} \tag{B.13}$$

$$V_{ri\mathrm{e}} = \Omega\,\sqrt{X_{ei}^2 + Y_{ei}^2} \tag{B.14}$$

$$G_\mathrm{e} = \tau H_\mathrm{S} + (1-\tau)\,H_\mathrm{S}\mathrm{e}^{-|V_{ri\mathrm{e}}/V_\mathrm{s}|^2} \tag{B.15}$$

Appendix C Linearised terms

$$\mathbf{K}_\mathrm{l} = \begin{bmatrix} K_\mathrm{p} - \sum_i \frac{\partial F_{fi\mathrm{Xe}}}{\partial X_1}, & -\sum_i \frac{\partial F_{fi\mathrm{Ye}}}{\partial Y_1}, & -\sum_i \frac{F_{fi\mathrm{Xe}}}{\partial \Theta}, & -\sum_i \frac{\partial F_{fi\mathrm{Xe}}}{\partial X_2}, & -\sum_i \frac{\partial F_{fi\mathrm{Xe}}}{\partial Y_2}, & -\sum_i \frac{\partial F_{fi\mathrm{Xe}}}{\partial \Phi} \\ -\sum_i \frac{\partial F_{fi\mathrm{Ye}}}{\partial X_1}, & K_\mathrm{p} - \sum_i \frac{\partial F_{fi\mathrm{Ye}}}{\partial Y_1}, & -\sum_i \frac{\partial F_{fi\mathrm{Ye}}}{\partial \Theta}, & -\sum_i \frac{\partial F_{fi\mathrm{Ye}}}{\partial X_2}, & -\sum_i \frac{\partial F_{fi\mathrm{Ye}}}{\partial Y_2}, & -\sum_i \frac{\partial F_{fi\mathrm{Ye}}}{\partial \Phi} \\ K_{31}, & K_{32}, & K_{33}, & K_{34}, & K_{35}, & K_{36} \\ \sum_i \frac{\partial F_{fi\mathrm{Xe}}}{\partial X_1}, & \sum_i \frac{\partial F_{fi\mathrm{Xe}}}{\partial Y_1}, & \sum_i \frac{F_{fi\mathrm{Xe}}}{\partial \Theta}, & K_\mathrm{d} + \sum_i \frac{\partial F_{fi\mathrm{Xe}}}{\partial X_2}, & \sum_i \frac{\partial F_{fi\mathrm{Xe}}}{\partial Y_2}, & \sum_i \frac{\partial F_{fi\mathrm{Xe}}}{\partial \Phi} \\ \sum_i \frac{\partial F_{fi\mathrm{Ye}}}{\partial X_1}, & \sum_i \frac{\partial F_{fi\mathrm{Ye}}}{\partial Y_1}, & \sum_i \frac{\partial F_{fi\mathrm{Ye}}}{\partial \Theta}, & \sum_i \frac{\partial F_{fi\mathrm{Ye}}}{\partial X_2}, & K_\mathrm{d} + \sum_i \frac{\partial F_{fi\mathrm{Ye}}}{\partial Y_2}, & \sum_i \frac{\partial F_{fi\mathrm{Ye}}}{\partial \Phi} \\ K_{61}, & K_{62}, & K_{63}, & K_{64}, & K_{65}, & K_{66} \end{bmatrix} \tag{C.1}$$

$$K_{31} = \sum_i [-\frac{\partial F_{fi\mathrm{Ye}}}{\partial X_1}\rho_i \cos(\gamma_i + \Theta_\mathrm{e}) + \frac{\partial F_{fi\mathrm{Xe}}}{\partial X_1}\rho_i \sin(\gamma_i + \Theta_\mathrm{e})], \tag{C.2}$$

$$K_{32} = \sum_i [-\frac{\partial F_{fi\mathrm{Ye}}}{\partial Y_1}\rho_i \cos(\gamma_i + \Theta_\mathrm{e}) + \frac{\partial F_{fi\mathrm{Xe}}}{\partial Y_1}\rho_i \sin(\gamma_i + \Theta_\mathrm{e})], \tag{C.3}$$

$$K_{33} = K_{\mathrm{p}\Theta} + \sum_i [\frac{\partial F_{fi\mathrm{Ye}}}{\partial \Theta}\rho_i \cos(\gamma_i + \Theta_\mathrm{e}) + F_{fi\mathrm{Ye}}\rho_i \sin(\gamma_i + \Theta_\mathrm{e}) + \frac{F_{fi\mathrm{Xe}}}{\partial \Theta}\rho_i \sin(\gamma_i + \Theta_\mathrm{e}) + F_{fi\mathrm{Xe}}\rho_i \cos(\gamma_i + \Theta_\mathrm{e})], \tag{C.4}$$

$$K_{34} = \sum_i [-\frac{\partial F_{fi\mathrm{Ye}}}{\partial X_2}\rho_i \cos(\gamma_i + \Theta_\mathrm{e}) + \frac{\partial F_{fi\mathrm{Xe}}}{\partial X_2}\rho_i \sin(\gamma_i + \Theta_\mathrm{e})] \tag{C.5}$$

$$K_{35} = \sum_i [-\frac{\partial F_{fi\mathrm{Ye}}}{\partial Y_2}\rho_i \cos(\gamma_i + \Theta_\mathrm{e}) + \frac{\partial F_{fi\mathrm{Xe}}}{\partial Y_2}\rho_i \sin(\gamma_i + \Theta_\mathrm{e})] \tag{C.6}$$

$$K_{36} = \sum_i [-\frac{\partial F_{fi\mathrm{Ye}}}{\partial \Phi}\rho \cos(\gamma_i + \Theta_\mathrm{e}) + \frac{\partial F_{fi\mathrm{Xe}}}{\partial \Phi}\rho_i \sin(\gamma_i + \Theta_\mathrm{e})] \tag{C.7}$$

$$K_{61} = \sum_i (\frac{\partial F_{fi\mathrm{Ye}}}{\partial X_1}X_{\mathrm{e}i} + F_{fi\mathrm{Ye}} - \frac{\partial F_{fi\mathrm{Xe}}}{\partial X_1}Y_{\mathrm{e}i}) \tag{C.8}$$

$$K_{62} = \sum_i (\frac{\partial F_{fi\mathrm{Ye}}}{\partial Y_1}X_{\mathrm{e}i} - \frac{\partial F_{fi\mathrm{Xe}}}{\partial Y_1}Y_{\mathrm{e}i}) - F_{fi\mathrm{Xe}} \tag{C.9}$$

$$K_{63} = \sum_i [\frac{\partial F_{fi\mathrm{Ye}}}{\partial \Theta}X_{\mathrm{e}i} - F_{fi\mathrm{Ye}}\rho_i \sin(\gamma_i + \Theta_\mathrm{e}) - \frac{\partial F_{fi\mathrm{Xe}}}{\partial \Theta}Y_{\mathrm{e}i} - F_{fi\mathrm{Xe}}\rho \cos(\gamma_i + \Theta_\mathrm{e})] \tag{C.10}$$

$$K_{64} = \sum_i (\frac{\partial F_{fi\mathrm{Ye}}}{\partial X_2}X_{\mathrm{e}i} - F_{fi\mathrm{Ye}} - \frac{\partial F_{fi\mathrm{Xe}}}{\partial X_2}Y_{\mathrm{e}i}) \tag{C.11}$$

$$K_{65} = \sum_i (\frac{\partial F_{fi\mathrm{Ye}}}{\partial Y_2}X_{\mathrm{e}i} - \frac{\partial F_{fi\mathrm{Xe}}}{\partial Y_2}Y_{\mathrm{e}i} + F_{fi\mathrm{Xe}}) \tag{C.12}$$

$$K_{66} = K_{\mathrm{d}\Phi} + \sum_i (\frac{\partial F_{fi\mathrm{Ye}}}{\partial \Phi}X_{\mathrm{e}i} - \frac{\partial F_{fi\mathrm{Xe}}}{\partial \Phi}Y_{\mathrm{e}i}) \tag{C.13}$$

$$\mathbf{C}_\mathrm{e} = \begin{bmatrix} C_\mathrm{p} - \sum_i \frac{\partial F_{fi\mathrm{Xe}}}{\partial \dot{X}_1}, & -\sum_i \frac{\partial F_{fi\mathrm{Ye}}}{\partial \dot{Y}_1}, & -\sum_i \frac{F_{fi\mathrm{Xe}}}{\partial \dot{\Theta}}, & -\sum_i \frac{\partial F_{fi\mathrm{Xe}}}{\partial \dot{X}_2}, & -\sum_i \frac{\partial F_{fi\mathrm{Xe}}}{\partial \dot{Y}_2}, & -\sum_i \frac{\partial F_{fi\mathrm{Xe}}}{\partial \dot{\Phi}} \\ -\sum_i \frac{\partial F_{fi\mathrm{Ye}}}{\partial \dot{X}_1}, & C_\mathrm{p} - \sum_i \frac{\partial F_{fi\mathrm{Ye}}}{\partial \dot{Y}_1}, & -\sum_i \frac{\partial F_{fi\mathrm{Ye}}}{\partial \dot{\Theta}}, & -\sum_i \frac{\partial F_{fi\mathrm{Ye}}}{\partial \dot{X}_2}, & -\sum_i \frac{\partial F_{fi\mathrm{Ye}}}{\partial \dot{Y}_2}, & -\sum_i \frac{\partial F_{fi\mathrm{Ye}}}{\partial \dot{\Phi}} \\ C_{31}, & C_{32}, & C_{33}, & C_{34}, & C_{35}, & C_{36} \\ \sum_i \frac{\partial F_{fi\mathrm{Xe}}}{\partial \dot{X}_1}, & \sum_i \frac{\partial F_{fi\mathrm{Xe}}}{\partial \dot{Y}_1}, & \sum_i \frac{F_{fi\mathrm{Xe}}}{\partial \dot{\Theta}}, & C_\mathrm{d} + \sum_i \frac{\partial F_{fi\mathrm{Xe}}}{\partial \dot{X}_2}, & \sum_i \frac{\partial F_{fi\mathrm{Xe}}}{\partial \dot{Y}_2}, & \sum_i \frac{\partial F_{fi\mathrm{Xe}}}{\partial \dot{\Phi}} \\ \sum_i \frac{\partial F_{fi\mathrm{Ye}}}{\partial \dot{X}_1}, & \sum_i \frac{\partial F_{fi\mathrm{Ye}}}{\partial \dot{Y}_1}, & \sum_i \frac{\partial F_{fi\mathrm{Ye}}}{\partial \dot{\Theta}}, & \sum_i \frac{\partial F_{fi\mathrm{Ye}}}{\partial \dot{X}_2}, & C_\mathrm{d} + \sum_i \frac{\partial F_{fi\mathrm{Ye}}}{\partial \dot{Y}_2}, & \sum_i \frac{\partial F_{fi\mathrm{Ye}}}{\partial \dot{\Phi}} \\ C_{61}, & C_{62}, & C_{63}, & C_{64}, & C_{65}, & C_{66} \end{bmatrix} \tag{C.14}$$

$$C_{31} = \sum_i [-\frac{\partial F_{fi\mathrm{Ye}}}{\partial \dot{X}_1}\rho_i \cos(\gamma_i + \Theta_\mathrm{e}) + \frac{\partial F_{fi\mathrm{Xe}}}{\partial \dot{X}_1}\rho_i \sin(\gamma_i + \Theta_\mathrm{e})], \tag{C.15}$$

$$C_{32} = \sum_i [-\frac{\partial F_{fi\mathrm{Ye}}}{\partial \dot{Y}_1}\rho_i \cos(\gamma_i + \Theta_\mathrm{e}) + \frac{\partial F_{fi\mathrm{Xe}}}{\partial \dot{Y}_1}\rho_i \sin(\gamma_i + \Theta_\mathrm{e})], \tag{C.16}$$

$$C_{33} = C_{\mathrm{p}\Theta} + \sum_i [-\frac{\partial F_{fi\mathrm{Ye}}}{\partial \dot{\Theta}}\rho_i \cos(\gamma_i + \Theta_\mathrm{e}) + \frac{\partial F_{fi\mathrm{Xe}}}{\partial \dot{\Theta}}\rho_i \sin(\gamma_i + \Theta_\mathrm{e})], \tag{C.17}$$

$$C_{34} = \sum_i [-\frac{\partial F_{fi\mathrm{Ye}}}{\partial \dot{X}_2}\rho_i \cos(\gamma_i + \Theta_\mathrm{e}) + \frac{\partial F_{fi\mathrm{Xe}}}{\partial \dot{X}_2}\rho_i \sin(\gamma_i + \Theta_\mathrm{e})], \tag{C.18}$$

$$C_{35} = \sum_i [-\frac{\partial F_{fi\mathrm{Ye}}}{\partial \dot{Y}_2}\rho_i \cos(\gamma_i + \Theta_\mathrm{e}) + \frac{\partial F_{fi\mathrm{Xe}}}{\partial \dot{Y}_2}\rho_i \sin(\gamma_i + \Theta_\mathrm{e})], \tag{C.19}$$

$$C_{36} = \sum_i [-\frac{\partial F_{fi\mathrm{Ye}}}{\partial \dot{\Phi}}\rho_i \cos(\gamma_i + \Theta_\mathrm{e}) + \frac{\partial F_{fi\mathrm{Xe}}}{\partial \dot{\Phi}}\rho_i \sin(\gamma_i + \Theta_\mathrm{e})], \tag{C.20}$$

$$C_{61} = \sum_i (\frac{\partial F_{fi\mathrm{Ye}}}{\partial \dot{X}_1} X_{\mathrm{e}i} - \frac{\partial F_{fi\mathrm{Xe}}}{\partial \dot{X}_1} Y_{\mathrm{e}i}), \tag{C.21}$$

$$C_{62} = \sum_i (\frac{\partial F_{fi\mathrm{Ye}}}{\partial \dot{Y}_1} X_{\mathrm{e}i} - \frac{\partial F_{fi\mathrm{Xe}}}{\partial \dot{Y}_1} Y_{\mathrm{e}i}), \tag{C.22}$$

$$C_{63} = \sum_i (\frac{\partial F_{fi\mathrm{Ye}}}{\partial \dot{\Theta}} X_{\mathrm{e}i} - \frac{\partial F_{fi\mathrm{Xe}}}{\partial \dot{\Theta}} Y_{\mathrm{e}i}), \tag{C.23}$$

$$C_{64} = \sum_i (\frac{\partial F_{fi\mathrm{Ye}}}{\partial \dot{X}_2} X_{\mathrm{e}i} - \frac{\partial F_{fi\mathrm{Xe}}}{\partial \dot{X}_2} Y_{\mathrm{e}i}), \tag{C.24}$$

$$C_{65} = \sum_i (\frac{\partial F_{fi\mathrm{Ye}}}{\partial \dot{Y}_2} X_{\mathrm{e}i} - \frac{\partial F_{fi\mathrm{Xe}}}{\partial \dot{Y}_2} Y_{\mathrm{e}i}), \tag{C.25}$$

$$C_{66} = C_{\mathrm{d}\Phi} + \sum_i (\frac{\partial F_{fi\mathrm{Ye}}}{\partial \dot{\Phi}} X_{\mathrm{e}i} - \frac{\partial F_{fi\mathrm{Xe}}}{\partial \dot{\Phi}} Y_{\mathrm{e}i}), \tag{C.26}$$

$$\frac{\partial F_{fi\mathrm{Xe}}}{\partial X_1} = -N_i\,\Omega\,(\frac{g_\mathrm{e}}{V_{\mathrm{r}i\mathrm{e}}V_\mathrm{s}} + \frac{G_\mathrm{e}}{V_{\mathrm{r}i\mathrm{e}}^3})V_{\mathrm{r}i\mathrm{X}}V_{\mathrm{r}i\mathrm{Y}} \tag{C.27}$$

$$\frac{\partial F_{fi\mathrm{Xe}}}{\partial \dot{X}_1} = -N_i\,(\frac{G_\mathrm{e}}{V_{\mathrm{r}i\mathrm{e}}} - \frac{g_\mathrm{e}V_{\mathrm{r}i\mathrm{X}}^2}{V_\mathrm{s}V_{\mathrm{r}i\mathrm{e}}} - \frac{G_\mathrm{e}V_{\mathrm{r}i\mathrm{X}}^2}{V_{\mathrm{r}i\mathrm{e}}^3} + \sigma_2) \tag{C.28}$$

$$\frac{\partial F_{fi\mathrm{Ye}}}{\partial Y_1} = -N_i\,\Omega\,(\frac{G_\mathrm{e}}{V_{\mathrm{r}i\mathrm{e}}} - \frac{g_eV_{\mathrm{r}i\mathrm{X}}^2}{V_{\mathrm{r}i\mathrm{e}}V_\mathrm{s}} - \frac{G_eV_{\mathrm{r}i\mathrm{X}}^2}{V_{\mathrm{r}i\mathrm{e}}^3} + \sigma_2) \tag{C.29}$$

$$\frac{\partial F_{fi\mathrm{Xe}}}{\partial \dot{Y}_1} = -N_i\,(-\frac{g_\mathrm{e}}{V_{\mathrm{r}i\mathrm{e}}V_\mathrm{s}} - \frac{G_\mathrm{e}}{V_{\mathrm{r}i\mathrm{e}}^3})V_{\mathrm{r}i\mathrm{X}}V_{\mathrm{r}i\mathrm{Y}} \tag{C.30}$$

$$\frac{F_{fi\mathrm{Xe}}}{\partial \Theta} = -Ni\,\Omega\rho_i\,[\frac{G_\mathrm{e}}{V_{\mathrm{r}i\mathrm{e}}}\cos(\gamma_i + \Theta_\mathrm{e}) - \frac{g_\mathrm{e}V_{\mathrm{r}i\mathrm{X}}}{V_{\mathrm{r}i\mathrm{e}}V_\mathrm{s}}(V_{\mathrm{r}i\mathrm{X}}\cos(\gamma_i + \Theta_\mathrm{e}) + V_{\mathrm{r}i\mathrm{Y}}\sin(\gamma_i + \Theta_\mathrm{e})) \tag{C.31}$$

$$- \frac{G_\mathrm{e}V_{\mathrm{r}i\mathrm{X}}}{V_{\mathrm{r}i\mathrm{e}}^3}(V_{\mathrm{r}i\mathrm{X}}\cos(\gamma_i + \Theta_\mathrm{e}) + V_{\mathrm{r}i\mathrm{Y}}\sin(\gamma_i + \Theta_\mathrm{e})) + \sigma_2\cos(\gamma_i + \Theta_\mathrm{e})] \tag{C.32}$$

$$\frac{\partial F_{fi\mathrm{Xe}}}{\partial \dot{\Theta}} = -N_i\rho_i[-(\frac{G_\mathrm{e}}{V_{\mathrm{r}i\mathrm{e}}} - \frac{g_\mathrm{e}V_{\mathrm{r}i\mathrm{X}}^2}{V_{\mathrm{r}i\mathrm{e}}V_\mathrm{s}} - \frac{G_\mathrm{e}V_{\mathrm{r}i\mathrm{X}}^2}{V_{\mathrm{r}i\mathrm{e}}^3} + \sigma_2)\sin(\gamma_i + \Theta_\mathrm{e}) - (\frac{g_\mathrm{e}}{V_{\mathrm{r}i\mathrm{e}}V_\mathrm{s}} + \frac{G_\mathrm{e}V_{\mathrm{r}i\mathrm{X}}^2}{V_{\mathrm{r}i\mathrm{e}}^3})V_{\mathrm{r}i\mathrm{X}}V_{\mathrm{r}i\mathrm{Y}}\cos(\gamma_i + \Theta_\mathrm{e})] \tag{C.33}$$

$$\frac{\partial F_{fi\mathrm{Xe}}}{\partial X_2} = -N_i\,\Omega\,(-\frac{-g_\mathrm{e}}{V_\mathrm{s}V_{\mathrm{r}i\mathrm{e}}} - \frac{G_\mathrm{e}}{V^3_{\mathrm{r}i\mathrm{e}}})V_{\mathrm{r}i\mathrm{X}}V_{\mathrm{r}i\mathrm{Y}}, \tag{C.34}$$

$$\frac{\partial F_{fi\mathrm{Xe}}}{\partial \dot{X}_2} = -N_i\,(-\frac{G_\mathrm{e}}{V_{\mathrm{r}i\mathrm{e}}} + \frac{g_\mathrm{e}V^2_{\mathrm{r}i\mathrm{X}}}{V_{\mathrm{r}i\mathrm{e}}V_\mathrm{s}} + \frac{G_\mathrm{e}V^2_{\mathrm{r}i\mathrm{X}}}{V^3_{\mathrm{r}i\mathrm{e}}} - \sigma_2), \tag{C.35}$$

$$\frac{\partial F_{fi\mathrm{Xe}}}{\partial Y_2} = -N_i\,\Omega\,(-\frac{G_\mathrm{e}}{V_{\mathrm{r}i\mathrm{e}}} + \frac{g_\mathrm{e}V^2_{\mathrm{r}i\mathrm{X}}}{V_{\mathrm{r}i\mathrm{e}}V_\mathrm{s}} + \frac{G_\mathrm{e}V^2_{\mathrm{r}i\mathrm{X}}}{V^3_{\mathrm{r}i\mathrm{e}}} - \sigma_2), \tag{C.36}$$

$$\frac{\partial F_{fi\mathrm{Xe}}}{\partial \dot{Y}_2} = -N_i\,(\frac{g_\mathrm{e}}{V_{\mathrm{r}i\mathrm{e}}V_\mathrm{s}} + \frac{G_\mathrm{e}}{V^3_{\mathrm{r}i\mathrm{e}}})V_{\mathrm{r}i\mathrm{X}}V_{\mathrm{r}i\mathrm{Y}}, \tag{C.37}$$

$$\frac{\partial F_{fi\mathrm{Xe}}}{\partial\, \Phi} = 0, \tag{C.38}$$

$$\frac{\partial F_{fi\mathrm{Xe}}}{\partial\, \dot{\Phi}} = -N_i\,[\frac{G_\mathrm{e}}{V_{\mathrm{r}i\mathrm{e}}}Y_{\mathrm{e}i} - \frac{g_\mathrm{e}V_{\mathrm{r}i\mathrm{X}}}{V_{\mathrm{r}i\mathrm{e}}V_\mathrm{s}}(V_{\mathrm{r}i\mathrm{X}}Y_{\mathrm{e}i} - V_{\mathrm{r}i\mathrm{Y}}X_{\mathrm{e}i}) - \frac{G_eV_{\mathrm{r}i\mathrm{X}}}{V^3_{\mathrm{r}i\mathrm{e}}}(V_{\mathrm{r}i\mathrm{X}}Y_{\mathrm{e}i} - V_{\mathrm{r}i\mathrm{Y}}X_{\mathrm{e}i}) + \sigma_2 Y_{\mathrm{e}i}], \tag{C.39}$$

$$\frac{\partial F_{fi\mathrm{Ye}}}{\partial X_1} = -N_i\,\Omega\,(-\frac{G_\mathrm{e}}{V_{\mathrm{r}i\mathrm{e}}} + \frac{g_eV^2_{\mathrm{r}i\mathrm{Y}}}{V_{\mathrm{r}i\mathrm{e}}V_\mathrm{s}} + \frac{G_eV^2_{\mathrm{r}i\mathrm{Y}}}{V^3_{\mathrm{r}i\mathrm{e}}} - \sigma_2), \tag{C.40}$$

$$\frac{\partial F_{fi\mathrm{Ye}}}{\partial \dot{X}_1} = -N_i\,(-\frac{g_\mathrm{e}}{V_{\mathrm{r}i\mathrm{e}}V_\mathrm{s}} - \frac{G_\mathrm{e}}{V^3_{\mathrm{r}i\mathrm{e}}})V_{\mathrm{r}i\mathrm{X}}V_{\mathrm{r}i\mathrm{Y}}, \tag{C.41}$$

$$\frac{\partial F_{fi\mathrm{Ye}}}{\partial Y_1} = -N_i\,\Omega\,(-\frac{g_\mathrm{e}}{V_{\mathrm{r}i\mathrm{e}}V_\mathrm{s}} - \frac{G_\mathrm{e}}{V^3_{\mathrm{r}i\mathrm{e}}})V_{\mathrm{r}i\mathrm{X}}V_{\mathrm{r}i\mathrm{Y}}, \tag{C.42}$$

$$\frac{\partial F_{fi\mathrm{Ye}}}{\partial \dot{Y}_1} = -N_i\,(-\frac{G_\mathrm{e}}{V_{\mathrm{r}i\mathrm{e}}} - \frac{g_eV^2_{\mathrm{r}i\mathrm{Y}}}{V_\mathrm{s}V_{\mathrm{r}i\mathrm{e}}} - \frac{G_eV^2_{\mathrm{r}i\mathrm{Y}}}{V^3_{\mathrm{r}i\mathrm{e}}} + \sigma_2), \tag{C.43}$$

$$\frac{\partial F_{fi\mathrm{Ye}}}{\partial\, \Theta} = -N_i\,\Omega\rho_i\,[\frac{G_\mathrm{e}}{V_{\mathrm{r}i\mathrm{e}}}\sin(\gamma_i + \Theta) - (\frac{g_eV_{\mathrm{r}i\mathrm{Y}}}{V_{\mathrm{r}i\mathrm{e}}V_\mathrm{s}} + \frac{G_eV_{\mathrm{r}i\mathrm{Y}}}{V^3_{\mathrm{r}i\mathrm{e}}})(V_{\mathrm{r}i\mathrm{X}}\cos(\gamma_i + \Theta_\mathrm{e}) + V_{\mathrm{r}i\mathrm{Y}}\sin(\gamma_i + \Theta)) + \sigma_2\sin(\gamma_i + \Theta_e)], \tag{C.44}$$

$$\frac{\partial F_{fi\mathrm{Ye}}}{\partial\, \dot{\Theta}_\mathrm{e}} = -N_i\,\rho_i\,[(\frac{G_\mathrm{e}}{V_{\mathrm{r}i\mathrm{e}}} - \frac{g_eV^2_{\mathrm{r}i\mathrm{Y}}}{V_{\mathrm{r}i\mathrm{e}}V_\mathrm{s}} - \frac{G_eV^2_{\mathrm{r}i\mathrm{Y}}}{V^3_{\mathrm{r}i\mathrm{e}}} + \sigma_2)\cos(\gamma_i + \Theta_\mathrm{e}) + (\frac{g_\mathrm{e}}{V_{\mathrm{r}i\mathrm{e}}V_\mathrm{s}} + \frac{G_\mathrm{e}}{V^3_{\mathrm{r}i\mathrm{e}}})V_{\mathrm{r}i\mathrm{X}}V_{\mathrm{r}i\mathrm{Y}}\sin(\gamma_i + \Theta_\mathrm{e})], \tag{C.45}$$

$$\frac{\partial F_{fi\mathrm{Ye}}}{\partial X_2} = -N_i\,\Omega\,(\frac{G_\mathrm{e}}{V_{\mathrm{r}i\mathrm{e}}} - \frac{g_eV^2_{\mathrm{r}i\mathrm{Y}}}{V_{\mathrm{r}i\mathrm{e}}V_\mathrm{s}} - \frac{G_eV^2_{\mathrm{r}i\mathrm{Y}}}{V^3_{\mathrm{r}i\mathrm{e}}} + \sigma_2), \tag{C.46}$$

$$\frac{\partial F_{fi\mathrm{Ye}}}{\partial \dot{X}_2} = -N_i\,(\frac{g_\mathrm{e}}{V_{\mathrm{r}i\mathrm{e}}V_\mathrm{s}} + \frac{G_\mathrm{e}}{V^3_{\mathrm{r}i\mathrm{e}}})V_{\mathrm{r}i\mathrm{X}}V_{\mathrm{r}i\mathrm{Y}}, \tag{C.47}$$

$$\frac{\partial F_{fi\mathrm{Ye}}}{\partial Y_2} = -N_i\,\Omega\,(\frac{g_\mathrm{e}}{V_{\mathrm{r}i\mathrm{e}}V_\mathrm{s}} + \frac{G_\mathrm{e}}{V^3_{\mathrm{r}i\mathrm{e}}})V_{\mathrm{r}i\mathrm{X}}V_{\mathrm{r}i\mathrm{Y}}, \tag{C.48}$$

$$\frac{\partial F_{fi\mathrm{Ye}}}{\partial \dot{Y}_2} = -N_i\,(-\frac{G_\mathrm{e}}{V_{\mathrm{r}i\mathrm{e}}} + \frac{g_eV^2_{\mathrm{r}i\mathrm{Y}}}{V^3_{\mathrm{r}i\mathrm{e}}} + \frac{G_eV^2_{\mathrm{r}i\mathrm{Y}}}{V^3_{\mathrm{r}i\mathrm{e}}} - \sigma_2), \tag{C.49}$$

$$\frac{\partial F_{fi\mathrm{Ye}}}{\partial\, \Phi} = 0, \tag{C.50}$$

$$\frac{\partial F_{fi\mathrm{Ye}}}{\partial\, \dot{\Phi}} = -N_i\,[-\frac{G_\mathrm{e}}{V_{\mathrm{r}i\mathrm{e}}}X_{\mathrm{e}i} - \frac{g_eV_{\mathrm{r}i\mathrm{Y}}}{V_{\mathrm{r}i\mathrm{e}}V_\mathrm{s}}(V_{\mathrm{r}i\mathrm{X}}Y_{\mathrm{e}i} - V_{\mathrm{r}i\mathrm{Y}}X_{\mathrm{e}i}) - \frac{G_eV_{\mathrm{r}i\mathrm{Y}}}{V^3_{\mathrm{r}i\mathrm{e}}}(V_{\mathrm{r}i\mathrm{X}}Y_{\mathrm{e}i} - V_{\mathrm{r}i\mathrm{Y}}X_{\mathrm{e}i}) - \sigma_2 X_{\mathrm{e}i}], \tag{C.51}$$

where

$$g_\mathrm{e} = 2(1-\tau)H_\mathrm{S}\mathrm{e}^{-|V_{\mathrm{r}i\mathrm{e}}/V_\mathrm{s}|^2} \tag{C.52}$$

References

[1] J. Kang, C. M. Krousgrill, F. Sadeghi, Comprehensive stability analysis of disc brake vibrations including gyroscopic, negative friction slope and mode-coupling mechanisms, Journal of Sound and Vibration 324 (1-2) (2009) 387–407. doi:10.1016/j.jsv.2009.01.050.

[2] H. Ouyang, J. E. Mottershead, M. P. Cartmell, M. I. Friswell, Friction-induced parametric resonances in discs: effect of a negative friction–velocity relationship, Journal of Sound and Vibration 209 (2) (1998) 251–264. doi:10.1006/jsvi.1997.1261.

[3] J.-J. Sinou, L. Jézéquel, Mode coupling instability in friction-induced vibrations and its dependency on system parameters including damping, European Journal of Mechanics-A/Solids 26 (1) (2007) 106–122. doi:10.1016/j.euromechsol.2006.03.002.

[4] N. Hoffmann, M. Fischer, R. Allgaier, L. Gaul, A minimal model for studying properties of the mode-coupling type instability in friction induced oscillations, Mechanics Research Communications 29 (4) (2002) 197–205. doi:10.1016/S0093-6413(02)00254-9.

[5] X. Wang, B. Huang, R. Wang, J. Mo, H. Ouyang, Friction-induced stick-slip vibration and its experimental validation, Mechanical Systems and Signal Processing 142 (2020) 106705.

[6] P. Gdaniec, C. Weiß, N. P. Hoffmann, On chaotic friction induced vibration due to rate dependent friction, Mechanics Research Communications 37 (2010) 92–95. doi:10.1016/j.mechrescom.2009.08.009.

[7] J. Kang, C. M. Krousgrill, The onset of friction-induced vibration and spragging, Journal of Sound and Vibration 329 (2010) 3537–3549. doi:10.1016/j.jsv.2010.03.002.

[8] J.-J. Sinou, F. Thouverez, L. Jezequel, Analysis of friction and instability by the centre manifold theory for a non-linear sprag-slip model, Journal of Sound and Vibration 265 (3) (2003) 527–559. doi:10.1016/S0022-460X(02)01453-0.

[9] R. Kikuuwe, N. Takesue, A. Sano, H. Mochiyama, H. Fujimoto, Fixed-step friction simulation: from classical coulomb model to modern continuous models, in: 2005 IEEE/RSJ International Conference on Intelligent Robots and Systems, IEEE, 2005, pp. 1009–1016. doi:10.1109/IROS.2005.1545579.

[10] N. Mostaghel, A non-standard analysis approach to systems involving friction, Journal of sound and vibration 284 (3-5) (2005) 583–595. doi:10.1016/j.jsv.2004.06.041.

[11] L. C. Bo, D. Pavelescu, The friction-speed relation and its influence on the critical velocity of stick-slip motion, Wear 82 (3) (1982) 277–289. doi:10.1016/0043-1648(82)90223-X.

[12] D. Karnopp, Computer simulation of stick-slip friction in mechanical dynamic systems (1985). doi:10.1115/1.3140698.

[13] P. R. Dahl, Solid friction damping of mechanical vibrations, AIAA journal 14 (12) (1976) 1675–1682. doi:10.2514/3.61511.

[14] C. Canudas De Wit, H. Olsson, K. J. Astrom, P. Lischinsky, A new model for control of systems with friction, IEEE Transactions on automatic control 40 (3) (1995) 419–425. doi:10.1109/9.376053.

[15] X. Lu, M. Khonsari, E. Gelinck, The stribeck curve: experimental results and theoretical prediction, Journal of tribology 128 (4) (2006) 789–794. doi:10.1115/1.2345406.

[16] W. Zhang, M. Li, Y. Gao, Y. Chen, Periodic adaptive learning control of pmsm servo system with lugre model-based friction compensation, Mechanism and Machine Theory 167 (2022) 104561. doi:10.1016/j.mechmachtheory.2021.104561.

[17] X. Tan, G. Chen, H. Shao, Modeling and analysis of spatial flexible mechanical systems with a spherical clearance joint based on the lugre friction model, Journal of Computational and Nonlinear Dynamics 15 (1) (2020) 011005. doi:10.1115/1.4045240.

[18] P. Dupont, B. Armstrong, V. Hayward, Elasto-plastic friction model: contact compliance and stiction, in: Proceedings of the 2000 American control conference. ACC (IEEE cat. no. 00CH36334), Vol. 2, IEEE, 2000, pp. 1072–1077. doi:10.1109/ACC.2000.876665.

[19] J. Swevers, F. Al-Bender, C. G. Ganseman, T. Projogo, An integrated friction model structure with improved presliding behavior for accurate friction compensation, IEEE Transactions on automatic control 45 (4) (2000) 675–686. doi:10.1109/9.847103.

[20] F. Marques, P. Flores, J. Pimenta Claro, H. M. Lankarani, A survey and comparison of several friction force models for dynamic analysis of multibody mechanical systems, Nonlinear Dynamics 86 (2016) 1407–1443. doi:10.1007/s11071-016-2999-3.

[21] E. Pennestrì, V. Rossi, P. Salvini, P. P. Valentini, Review and comparison of dry friction force models, Nonlinear dynamics 83 (2016) 1785–1801. doi:10.1007/s11071-015-2485-3.

[22] E. Velenis, P. Tsiotras, C. Canudas-de Wit, Extension of the lugre dynamic tire friction model to 2d motion, in: Proceedings of the 10th IEEE Mediterranean conference on control and automation-MED, 2002, pp. 9–12.

[23] Z. Zhou, X. Zheng, Q. Wang, Z. Chen, Y. Sun, B. Liang, Modeling and simulation of point contact multibody system dynamics based on the 2d lugre friction model, Mechanism and Machine Theory 158 (2021) 104244. doi:10.1016/j.mechmachtheory.2021.104244.

[24] N. Liu, H. Ouyang, Friction-induced vibration considering multiple types of nonlinearities, Nonlinear Dynamics 102 (2020) 2057–2075. doi:10.1007/s11071-020-06055-x.

[25] Z.-G. Song, F.-M. Li, Active aeroelastic flutter analysis and vibration control of supersonic beams using the piezoelectric actuator/sensor pairs, Smart Materials and Structures 20 (5) (2011) 055013. doi:10.1088/0964-1726/20/5/055013.

[26] P. Liu, H. Zheng, C. Cai, Y. Wang, C. Lu, K. Ang, G. Liu, Analysis of disc brake squeal using the complex eigenvalue method, Applied acoustics 68 (6) (2007) 603–615. doi:10.1016/j.apacoust.2006.03.012.

[27] G. Spelsberg-Korspeter, P. Hagedorn, Complex eigenvalue analysis and brake squeal: traps, shortcomings and their removal, SAE International Journal of Passenger Cars-Mechanical Systems 5 (2012-01-1814) (2012) 1211–1216. doi:10.4271/2012-01-1814.

[28] Z. Li, H. Ouyang, Z. Guan, Nonlinear friction-induced vibration of a slider-belt system, Journal of Vibration and Acoustics, Transactions of the ASME 138, bifurcation analysis is conducted regarding the real and imaginary parts of the eigenvalue (the first one?) (8 2016). doi:10.1115/1.4033256.

[29] T. Butlin, J. Woodhouse, Friction-induced vibration: Quantifying sensitivity and uncertainty, Journal of Sound and Vibration 329 (5) (2010) 509–526. doi:10.1016/j.jsv.2009.09.026.

[30] F. Massa, H. Q. Do, T. Tison, O. Cazier, Uncertain friction-induced vibration study: coupling of fuzzy logic, fuzzy sets, and interval theories, ASCE-ASME J Risk and Uncert in Engrg Sys Part B Mech Engrg 2 (1) (2016). doi:10.1115/1.4030469.

[31] L. Nechak, J. Sinou, Hybrid surrogate model for the prediction of uncertain friction-induced instabilities, Journal of Sound and Vibration 396 (2017) 122–143. doi:10.1016/j.jsv.2017.01.040.

[32] A. Nobari, H. Ouyang, P. Bannister, Statistics of complex eigenvalues in friction-induced vibration, Journal of Sound and Vibration 338 (2015) 169–183. doi:10.1016/j.jsv.2014.10.017.

[33] H. Hu, A. Batou, H. Ouyang, Coefficient of friction random field modelling and analysis in planar sliding, Journal of Sound and Vibration 508 (2021) 116197. doi:10.1016/j.jsv.2021.116197.

[34] H. Hu, A. Batou, H. Ouyang, Friction-induced vibration of a stick–slip oscillator with random field friction modelling, Mechanical Systems and Signal Processing 183 (2023) 109572. doi:10.1016/j.ymssp.2022.109572.

[35] P. J. Blau, The significance and use of the friction coefficient, Tribology International 34 (9) (2001) 585–591. doi:10.1016/S0301-679X(01)00050-0.

[36] R. K. Sivamani, J. Goodman, N. V. Gitis, H. I. Maibach, Coefficient of friction: tribological studies in man–an overview, Skin Research and Technology 9 (3) (2003) 227–234. doi:10.1034/j.1600-0846.2003.02366.x.

[37] D. Moens, M. De Munck, W. Desmet, D. Vandepitte, Numerical dynamic analysis of uncertain mechanical structures based on interval fields, in: IUTAM Symposium on the Vibration Analysis of Structures with Uncertainties:

Proceedings of the IUTAM Symposium on the Vibration Analysis of Structures with Uncertainties held in St. Petersburg, Russia, July 5–9, 2009, Springer, 2011, pp. 71–83. doi:10.1007/978-94-007-0289-9_6.

[38] A. Sofi, Structural response variability under spatially dependent uncertainty: stochastic versus interval model, Probabilistic Engineering Mechanics 42 (2015) 78–86. doi:10.1016/j.probengmech.2015.09.001.

[39] C. Jiang, B. Ni, X. Han, Y. Tao, Non-probabilistic convex model process: a new method of time-variant uncertainty analysis and its application to structural dynamic reliability problems, Computer Methods in Applied Mechanics and Engineering 268 (2014) 656–676. doi:10.1016/j.cma.2013.10.016.

[40] H. Hu, Y. Wu, A. Batou, H. Ouyang, B-spline based interval field decomposition method, Computers & Structures 272 (2022) 106874. doi:10.1016/j.compstruc.2022.106874.

[41] N. Liu, H. Ouyang, Friction-induced planar vibration of two rigid plates, Applied Mathematical Modelling (2022). doi:10.1016/j.apm.2022.05.015.

[42] F. Marques, Ł. Woliński, M. Wojtyra, P. Flores, H. M. Lankarani, An investigation of a novel lugre-based friction force model, Mechanism and Machine Theory 166 (2021) 104493. doi:10.1016/j.mechmachtheory.2021.104493.

[43] K. Johanastrom, C. Canudas-de Wit, Revisiting the lugre friction model, IEEE Control Systems Magazine 28 (6) (2008) 101–114. doi:10.1109/MCS.2008.929425.

[44] L. F. Shampine, M. W. Reichelt, The matlab ode suite, SIAM journal on scientific computing 18 (1) (1997) 1–22. doi:10.1137/S1064827594276424.

[45] Z. Li, H. Ouyang, Z. H. Wei, Insights into instability of friction-induced vibration of multi-degree-of-freedom models, Journal of Sound and Vibration 503 (7 2021). doi:10.1016/j.jsv.2021.116107.

[46] O. Ben-David, J. Fineberg, Static friction coefficient is not a material constant, Physical review letters 106 (25) (2011) 254301. doi:10.1103/PhysRevLett.106.254301.

[47] Q. Feng, A discrete model of a stochastic friction system, Computer methods in applied mechanics and engineering 192 (20-21) (2003) 2339–2354. doi:10.1016/S0045-7825(03)00241-X.

[48] T. Ritto, M. Escalante, R. Sampaio, M. B. Rosales, Drill-string horizontal dynamics with uncertainty on the frictional force, Journal of Sound and Vibration 332 (1) (2013) 145–153. doi:10.1016/j.jsv.2012.08.007.